DIGITAL ACCESS TO SCHOLARSHIP AT HARVARD
DASH.HARVARD.EDU

HARVARD LIBRARY
Office for Scholarly Communication

A bioelectrical phase transition patterns the first vertebrate heartbeats

Citation

Jia, Bill, Yitong Qi, J. David Wong-Campos, Sean Megason, Adam E. Cohen. "A bioelectrical phase transition patterns the first vertebrate heartbeats." Nature 622, no. 7981 (2023): 149-155. DOI: 10.1038/s41586-023-06561-z

Permanent link

https://nrs.harvard.edu/URN-3:HUL.INSTREPOS:37377526

Terms of Use

This article was downloaded from Harvard University's DASH repository, and is made available under the terms and conditions applicable to Other Posted Material, as set forth at http://nrs.harvard.edu/urn-3:HUL.InstRepos:dash.current.terms-of-use#LAA

Share Your Story

The Harvard community has made this article openly available.
Please share how this access benefits you. Submit a story .

Accessibility

A bioelectrical phase transition patterns the first vertebrate heartbeats

Bill Z. Jia[1,2,3], Yitong Qi[1], J. David Wong-Campos[1], Sean G. Megason[2]*, Adam E. Cohen[1,4]*

Abstract

A regular heartbeat is essential to vertebrate life. In the mature heart this function is driven by an anatomically localized pacemaker. In contrast, pacemaking capability is broadly distributed in the early embryonic heart[1–3], raising the question of how tissue-scale organization of activity is first established and then maintained during embryonic development. The initial transition of the heart from silent to beating has never been characterized at the timescale of individual electrical events, and the structure in space and time of the early heartbeats remains poorly understood. Using all-optical electrophysiology, we captured the very first zebrafish heartbeat and analyzed the development of cardiac excitability and conduction around this singular event. The first beats appeared suddenly, had irregular inter-beat intervals, propagated coherently across the primordial heart, and emanated from loci that varied between animals and over time. The bioelectrical dynamics were well described by a noisy saddle-node on invariant circle (SNIC) bifurcation with action potential upstroke driven by $Ca_V1.2$. Our work shows how gradual and largely asynchronous development of single-cell bioelectrical properties produces a stereotyped and robust tissue-scale transition from quiescence to coordinated beating.

Main

Cardiac activity during early embryonic development has been documented for over two thousand years[4,5]. However, *in vivo* observations of physiological function in the heart primordium have been limited in spatiotemporal resolution and sample size[6–11]. This scarcity of data means that the bioelectrical mechanisms for the emergence of organized cardiac function are still poorly understood. We asked: how does the heart go from silent to regular beating? What are the intermediate activity states, and how do these states emerge from the ensemble of single-cell developmental trajectories[12]? Here, we applied all-optical electrophysiology[13] to observe the first beats of developing zebrafish hearts and to assess the electrical excitability and connectivity patterns underlying these dynamics.

Capturing the first heartbeat

A first heartbeat is a once-in-a-lifetime event. We sought to capture this event via calcium imaging as zebrafish embryos developed from 18 – 22 hours post fertilization (hpf; Fig. 1a). During this period, the bilateral cardiac progenitor populations converge and form the heart cone, and early heartbeats have been reported at homologous developmental stages in the chick, rat, and mouse[6–11]. At this stage, the progenitors are differentiating into distinct cell types, so we ubiquitously expressed the genetically encoded calcium indicator (GECI) jGCaMP7f[14] to capture activity that might be missed by tissue-specific expression. To acquire robust statistics, we combined a system for wide-area all-optical electrophysiology[15] with a custom agarose mold for live imaging of up to 18 embryos concurrently (Fig. 1b; Supplementary File 1; Supplementary Videos 1,2; Methods). This system produced consistent recordings across experiments (Extended Data Fig. 1a). Commonly used tools for arresting cardiac and skeletal muscle motion (*tnnt2a* morpholino and alpha-bungarotoxin mRNA respectively) had little effect on the calcium activity (Extended Data Fig. 1b–d). A second red-shifted GECI, FR-GECO1c[16], also recorded similar dynamics and time of initiation (Extended Data Fig. 1e–g). Dynamics were uncorrelated between neighboring embryos, implying minimal mechanical or chemical coupling (Extended Data Fig. 1h). These results establish that our experimental preparation faithfully captured the early development of zebrafish cardiac physiology.

[1]Department of Chemistry and Chemical Biology, Harvard University. [2]Department of Systems Biology, Blavatnik Institute, Harvard Medical School. [3]Systems, Synthetic and Quantitative Biology Ph.D. Program, Harvard University. [4]Department of Physics, Harvard University. * co-corresponding authors: megason@hms.harvard.edu, cohen@chemistry.harvard.edu.

Within each embryo, the primordial heart showed an abrupt transition from quiescence to calcium spiking with a stereotyped waveform. These transitions occurred in a tight developmental window of 20.3 ± 0.4 hpf (mean ± SD, n = 39 embryos; Fig. 1c–e, Methods). Calcium dynamics mostly colocalized with fluorescent protein reporters in *Tg(myl7:eGFP)*[17] and *Tg(-36nkx2.5:ZsYellow)*[18] lines, suggesting that the activity occurred in developing cardiomyocytes (Extended Data Fig. 2a–c). Consistent with previous reports, rhythmic calcium dynamics were present before mechanical contractions could be detected (typically 21–22 hpf) using brightfield microscopy (Supplementary Videos 3,4)[7,8,11]. We refer to the first large-scale calcium transient as the first heartbeat.

We next asked whether the first heartbeat engaged the whole tissue or was confined to a subset of cells. Prior to the first heartbeat, we observed occasional single-cell calcium transients, as has been reported previously[11]. These events were infrequent (0.2 – 0.7 per minute), long-lived (3.40 ± 2.09 s), lacked a sharp peak, and were asynchronous between cells, making them qualitatively distinct from the first heartbeats (Fig. 2a; Extended Data Fig. 3a–d). The first beat usually engaged > 4000 μm^2 of tissue, comprising most of the heart primordium, compared to a typical cell size of 82 μm^2 (Extended Data Fig. 3e–f; Supplementary Video 5). However, the first beat occasionally (3/39) preceded the electrical fusion of the two progenitor fields and only propagated through half of the heart (Fig. 2a; Extended Data Fig. 3g–i). In such cases, the beat engaged the contralateral side within 30 minutes. During the hour after the first beat, the spatial extent of the spikes and the spatially averaged spike amplitude only increased slightly (area: 35 ± 47% increase, amplitude: 22 ± 27% increase) and spike width only decreased slightly (-24 ± 10% decrease), (Fig. 2b–d; Extended Data Fig. 3j–o). Therefore, the initiation of the heartbeat was a step change from sparse and slow single-cell transients to sharp, tissue-scale spikes that remained relatively stable in spatial extent and waveform over the following hour of development.

Tissue-average dynamics of the early heartbeat

We then investigated how the heartbeat became periodic. The first beats were infrequent and irregularly spaced. The inter-spike interval (ISI) became shorter and more uniform as the heart developed (Fig. 2e). The heart rate increased from 7.1 ± 3.3 beats per minute (bpm) at 10 minutes post onset (mpo) to 29.6 ± 7.9 bpm at 120 mpo (Fig. 2f). We quantified the heart rate variability by the coefficient of variation (CV: standard deviation/mean) of the ISI. This ISI CV decreased from 0.62 (0.44–0.83) (denoted as: "median (interquartile range, IQR)" throughout the text) at 10 mpo (ISI CV = 1 corresponds to a Poisson process) to 0.37 (0.26–0.52) at 120 mpo (Fig. 2g).

Excitable-to-oscillatory phase transition

The mean heart rate and ISI CV of individual embryos followed stereotyped trajectories when aligned temporally to the first beat, suggesting a characteristic transition underlying the dynamics (Fig. 2f, g). We thus sought to understand the nature of the transition from quiescence to beating. This transition can be described as a codimension-1 bifurcation, i.e. a step change in dynamics driven by a continuous change in a control parameter. There are just four classes of codimension-1 bifurcations into an oscillatory state[19]. The class of bifurcation determines an oscillator's qualitative dynamics, including oscillation amplitude, frequency, and stability, as well as its response to perturbations. Efforts to classify bifurcations in biological oscillators have yielded important insights into physiological function, e.g. in the computational properties of neurons[19–21] and the sensing mechanisms of cochlear hair cells[22]. We therefore sought to assign the initiation of the heartbeat to one of these classes.

We compared our experimental results to simulated excitable-to-oscillatory transitions, using the action potential model of Morris and Lecar, which is the simplest model that allows simulation of all four bifurcation types (Supplementary Information; Extended Data Fig. 4a,b)[23]. To capture the beat-rate variability in the system, we added white noise to the drive current. Interestingly, only the saddle-node on invariant circle (SNIC) bifurcation captured the experimental spike timing statistics (Extended Data Fig. 4c). The other bifurcations also differed qualitatively from the data (Supplementary Information), showing graded oscillation amplitude (supercritical Hopf bifurcation) or bistability between oscillatory and silent states (saddle-node, subcritical Hopf bifurcations). In contrast, the SNIC bifurcation predicted a relatively constant spike amplitude near the bifurcation point, and an absence of bistability between silent and spiking states, both consistent with our data.

All SNIC bifurcation models have similar dynamics near the bifurcation point[24], so we proceeded with the simplest, the quadratic integrate-and-fire (QIF) model[19] (Supplementary Information). The noisy QIF model comprises just a "spiking" variable, φ, and two free parameters, the "injected current", *I,* and the noise power, σ_w^2. Intuitively, *I* determines the distance between a stable resting state and an excitation threshold. When φ crosses the excitation threshold, φ spikes and then returns to the resting state (Extended Data Fig. 4d – e). As *I* increases, the resting state and excitation threshold get closer until they annihilate each other, yielding the transition from excitable to oscillatory. Strikingly, within a range of values of σ_w^2, the noisy QIF model captured the evolution of both mean beat frequency and ISI CV with just a linear scaling of *I* to developmental time (Fig. 2h – j; Extended Data Fig. 5a – c). The QIF model also reproduced probability distributions and autocorrelation functions of experimental ISIs (Extended Data Fig. 5d – g). In summary, the periodic heartbeat emerges through a phase transition-like SNIC bifurcation, bridged by a regime of noisy spontaneous spiking (Fig. 2k, l).

Calcium-voltage coupling

The SNIC bifurcation suggests that early calcium transients arose by noisy crossing of an excitation threshold, followed by positive feedback amplification. The threshold and positive feedback could come from voltage-dependent ion channels, e.g. voltage-gated calcium channels (VGCCs), or from voltage-independent intracellular mechanisms, e.g. calcium-induced calcium release[25,26]. To distinguish these possibilities, we generated a transgenic zebrafish line co-expressing jGCaMP7f and a voltage indicator, Voltron1[27], in the heart primordium (Fig. 3a). To improve expression in the heart primordium, we developed a novel chimeric promoter (*zACNE20-myl7* (*z20m*); Extended Data Fig. 6). Expression under *z20m* co-localized with *myl7* mRNA and pan-myosin heavy chain antibody (MF-20), markers for myocardium (Extended Data Fig. 6). We used a dual-wavelength imaging system and a red-shifted HaloTag ligand dye to simultaneously capture V_{mem} and calcium activity in *Tg(z20m:Voltron1-P2A-jGCaMP7f)* embryos (Fig. 3b–d; Supplementary Video 6).

After the onset of beating, there was a 1:1 relation between spikes in V_{mem} and in calcium. The electrical upstroke preceded the Ca2+ upstroke by 97 (76 – 131) ms (Fig. 3c, e), longer than the difference in sensor kinetics (Voltron1 and jGCaMP7f have half-rise times of 0.44 ms and 27 ms respectively). Both voltage and Ca^{2+} propagated through the tissue as coherent waves, with Ca^{2+} lagging V_{mem} in space (Fig. 3d; Supplementary Video 6), consistent with our previously observed tissue-scale initiation of the heartbeat (Fig. 2a; Extended Data Fig. 3; Supplementary Video 5). We did not observe any voltage spikes above baseline noise prior to the onset of Ca^{2+} spiking (Fig. 3b; Extended Data Fig. 1k–o ; Methods). These results establish that the first beats comprise electrical action potentials.

Since calcium elevation followed voltage depolarization, we probed the role of VGCCs in driving the early dynamics. We performed morpholino knockdown of *cacna1c*, which encodes the pore-forming α1c subunit of the L-type VGCC $Ca_V1.2$[28]. In *cacna1c* morphants, neither calcium transients nor electrical action potentials (APs) could be detected by 22 – 23 hpf (Fig. 3f, g; Extended Data Fig. 7a–c). This finding points to $Ca_V1.2$ as the dominant channel for the earliest AP upstrokes, consistent with pharmacological studies in 36 hpf fish[29] and early mouse hearts[11,30].

We further investigated several other transporters which are important for electrical automaticity in adult pacemaker cardiomyocytes (Extended Data Fig. 7d–h). Morpholino knockdown of the sodium-calcium exchanger *ncx1* slowed the decay of the earliest calcium transients and eventually generated long calcium plateaus, consistent with its role in removing excess calcium from the cytosol. In more mature pacemaker cells, intracellular Ca^{2+} fluctuations are thought to contribute to spontaneous spiking via an NCX1-mediated current[30,31]. Knockdown of *ncx1* did not delay the first calcium transients (Extended Data Fig. 7e), suggesting that this mechanism is not yet active in the first heartbeats.

Morpholino knockdown of *hcn4*, which generates the hyperpolarization-activated "funny current"[32], also did not delay the first beats and furthermore had no effect on spontaneous calcium dynamics (Extended Data Fig. 7f–h). This observation is consistent with a prior report that the funny current only becomes active between 54 and 102 hpf[29]. Knockdown of *atp1a1a,* a subunit of the Na^+,K^+-ATPase important for regulating resting V_{mem}[33], delayed initiation and slowed the acceleration of heart rate, consistent with a view that electrical polarization is necessary for the first beats. Together, these experiments establish depolarization-activated transmembrane Ca^{2+} currents as the driver of the first beats.

Development of electrical excitability and conduction

A key prediction of the SNIC bifurcation model is that it should become increasingly easy to excite action potentials in the time approaching the first spontaneous beats, as the baseline V_{mem} and threshold approach each other (Fig. 2k, l). To test this prediction, we used the channelrhodopsin CoChR[34] to optogenetically depolarize the heart primordium while imaging with FR-GECO1c (Fig. 4a). We applied periodic impulses of blue light targeted to the whole heart and measured the probability of evoking a calcium transient as a function of developmental time (Fig. 4b; Supplementary Video 2). We observed all-or-none responses to individual stimuli, indicative of coherent tissue-wide responses which resembled later spontaneous heartbeats. The heart became optogenetically excitable in a window 90 minutes before the first spontaneous beats (Fig. 4b–d). Within individual embryos, the response rate to optogenetic stimuli increased from 0% to close to 100% in typically less than 5 minutes. This rapid transition is qualitatively consistent with the phase transition-like behavior observed in the endogenous dynamics (Fig. 1e, f; Fig. 1f–i). Optogenetic stimulus before spontaneous beating did not affect when the heart subsequently started beating spontaneously or its rate (Extended Data Fig. 1i–j). Optogenetic stimuli did not evoke beats in *cacna1c* morphant fish (Extended Data Fig. 7i–j), consistent with the key role for $Ca_v1.2$ in driving the early action potential.

To understand how the first heartbeats typically engaged the entire heart field (Supplementary Video 5), we investigated the nature of cell coupling before the first beats. During the epoch where the heart was excitable but not yet spontaneously active, we targeted optogenetic stimuli to small sub-regions of the heart in *Tg(z20m:FRGECO1c-P2A-CoChR-eGFP)* fish. These stimuli elicited propagating calcium waves that initiated at the stimulus location (Fig. 4e; Supplementary Video 7). Therefore, cells were coupled before the initiation of the spontaneous heartbeat and could be excited not only by external stimuli but also by their neighbors. Wave propagation speeds were similar between precocious optically evoked waves, 617 (567–767) μm/s, and early spontaneous activity, 646 (465–772) μm/s, (n.s., Fig. 4f). These speeds were an order of magnitude faster than reported values for calcium waves driven by diffusion of small molecules[35]. Immunofluorescence showed expression of the gap junction protein connexin-43 as early as 18 hpf (Extended Data Fig. 8). These observations combined with our measurements of voltage excitability and AP propagation (Fig. 3d) suggest that wave propagation was mediated by sharing of V_{mem} between cells, consistent with gap junction coupling. The presence of both electrical excitability and coupling thus primes the heart for a tissue-wide response to the first spontaneous action potential, explaining the sudden transition from silence to large-area coherent heartbeats.

Spatial origins of electrical waves

The capacity for spontaneous activity is widespread in embryonic cardiomyocytes and gradually becomes localized to cells in molecularly distinct pacemaker regions during development[1–3]. Reports on the spatial locus of initiation (LOI) of early heartbeats vary[6–8], and the mechanisms determining its location in the early heart are unknown. To locate the early LOI in zebrafish hearts, we made high-speed (100 Hz) calcium-imaging maps of the spontaneous heartbeats at 20-22 hpf, using the jGCaMP7f reporter (Fig. 5a; Methods). The LOI was variable in location between embryos (Fig. 5b) with a bias for the anterior-left quadrant of the heart cone (38/71 observations across 10 embryos). The LOI was typically stable for >10 minutes, but large and sudden displacements of the LOI (> 200 μm/h) between recordings occurred occasionally (mean 1 event/70 min; Extended Data Fig. 2d).

We sought to relate the functional LOI to the underlying pattern of cell identities. The zebrafish heart cone has a well-defined fate map, with distal regions of the cone contributing to the inflow tract, pacemakers, and atrium, and proximal regions contributing to the ventricle and outflow tract[36,37]. The early LOI (15 – 45 mpo) resided primarily in the proximal heart cone and colocalized with *myl7:eGFP* (Extended Data Fig. 2e,f). The LOI drifted outwards as development progressed (15 mpo: 29 (25–31) μm from the inner edge; 105 mpo: 54 (44–65) μm; Fig. 5a–c). Consistent with its anatomical trajectory, the initial LOI expressed *nkx2.5:ZsYellow* more strongly than the later LOI (Fig. 5d).

The proximal Nkx2.5+ location (Extended Data Fig. 2g) of the initial LOI contrasts with the concurrent specification of a reported pacemaker lineage in a distal (~100 μm outwards) and sparse Isl1+/TCF+ population undergoing downregulation of Nkx2.5[37]. At later stages (~22 hpf), the LOI was located in a region of TCF+ cells (Fig. 5a) with reduced *nkx2.5:ZsYellow* fluorescence (Fig. 5d). There is little cell mixing during zebrafish heart tube formation (Supplementary Video 8, refs. [38,39]), confirming that the relative positions of different cell fates

are preserved. Consistent with this notion, relative *nkx2.5:ZsYellow* intensity at the original location of the LOI at 15 mpo was unchanged at 105 mpo (Extended Data Fig. 2h). These observations imply that the LOI moved between cell populations. In summary, the location of the early LOI is not precisely specified, but it is preferentially located in the future ventricular myocardium. This location is spatially distinct from the cells that ultimately become pacemakers.

Dynamical determinants of LOI position

The SNIC model predicts that the spontaneous frequency depends strongly on the bifurcation parameter. Within a tissue where there are gradients and spatial variability in developmental trajectories (Fig. 5a – d), one would expect a diversity of spontaneous frequencies. How, then, does the tissue produce coherent beats that emerge from a relatively stable LOI?

We hypothesized that electrical coupling between cells led to phase locking to the highest frequency oscillator. To test this hypothesis, we used the hyperpolarizing anion channelrhodopsin gtACR2[40] and targeted illumination to selectively silence different regions of the heart (Fig. 5e–h; Supplementary Video 9), while simultaneously monitoring calcium with FR-GECO1c. Silencing of the LOI caused a drop in spontaneous frequency, f, and the emergence of a new LOI in a different spot, whereas silencing non-LOI regions caused significantly smaller relative frequency drops (f_{after}/f_{before}: LOI silenced, 0.870 (0.663–1.0657); non-LOI region silenced, 1.15 (0.96–1.25)) and little LOI displacement (LOI silenced: 70.46 (476.59–87.19) μm; non-LOI region silenced: 25 (15–46) μm; Fig. 5i, j; Supplementary Video 9). These observations indicate the presence of multiple potential LOIs, with the actual wave origin set by the one with the fastest natural frequency. This mechanism resembles the "overdrive suppression" that determines heartbeat initiation site in the adult cardiac conduction system[41]. The presence of overdrive suppression is consistent with prior suggestions based on experiments in dissociated embryonic cardiomyocytes and surgically or genetically perturbed hearts[6,42,43], but to our knowledge has not previously been identified in the intact embryonic heart.

We further tested the overdrive suppression model by focal CoChR pacing of spontaneously active hearts at different frequencies. The optogenetic stimuli only changed beat rate and LOI position when the stimulus frequency was faster than the spontaneous frequency (Extended Data Fig. 9). Furthermore, once pacing stopped, the LOI immediately returned to its previous rhythm and location, with no apparent memory of pacing (Extended Data Fig. 9). The presence of relatively stable LOI locations and an outward drift punctuated by occasional jumps suggests competition among multiple cellular oscillators, each with asynchronous maturation toward gradually increasing spontaneous beat rate.

Robustness to noisy patterning of electrical properties

We then asked whether a spatially extended model of an excitable-to-oscillatory transition could account for the above observations on LOI position and response to perturbations. We simulated resistively coupled Morris-Lecar oscillators undergoing a SNIC bifurcation, with a linear spatial gradient of input current, I, to model the observed clustering of the LOI in the anterior-left quadrant. Despite dynamic current noise and static heterogeneity of excitability, the simulations produced coherent waves which emerged from a single LOI and swept the tissue under a broad range of parameters (Supplementary Information; Extended Data Fig. 10). A time-dependent offset in the current recapitulated the beat-rate statistics, as in the single-oscillator QIF model (Extended Data Fig. 10; Fig. 2f – j). Thus, our model can explain how noisy and gradually changing single-cell excitability properties can produce abrupt and tissue-wide changes in action potential dynamics.

Discussion

Our work provides a coherent picture for how the heart starts beating **(**Fig. 5k). The heart becomes electrically coupled and excitable before the first spontaneous beats. Beating begins as the result of a SNIC bifurcation resulting in a sudden transition to full-fledged, $Ca_V1.2$-dependent action potentials that sweep the tissue. Overdrive suppression among many spontaneously active units in the proximal heart cone then assures the presence of one, and only one, locus of initiation in a single beat. The determination of the early LOI is not driven by a molecularly distinct "pacemaker" cell-type, but rather emerges by biophysical interaction of spatially distributed and noisy oscillators. Isl1+/Nkx2.5- pacemaker cells only begin to act as the LOI later in development.

The use of advanced optical electrophysiology tools in zebrafish allowed us to characterize this intricate process with high resolution in a minimally invasive way. We observed many features consistent with past studies in amniote embryos, including: asynchronous single-cell calcium transients before the first beats[11], major functional roles for VGCCs and NCX[11,30], electrical and calcium spikes before mechanical contractions[7,8,11], and variability and lability of the spatial origin of heartbeats[9]. These similarities suggest that many of the early events in heartbeat functional development are conserved across vertebrates. Our results unify these observations and identify how they contribute to the spatiotemporal organization of the earliest cardiac dynamics.

Our data show that the spatial structure of the first heartbeats undergoes a rapid step transition to tissue-scale engagement, but the temporal structure goes through a noisy intermediate between quiescence and periodicity. All biological dynamics are affected by noise, including oscillations[44] and bifurcations[45]. Living systems must overcome this variability to achieve order[46,47], but in many cases noise plays an important role in function[48]. The initiation of the zebrafish heartbeat falls into this latter category – remarkably, a simple, well-studied model[49] of a stochastic SNIC bifurcation captures all the dynamical steps between quiescence and regular beating.

The function of early self-organized electrical activity is unclear. A rhythmic, spatially structured beat arises well before connection to the circulatory system and blood pumping and is not necessary for survival in early zebrafish embryos[50]. Early activity may contribute to further cardiovascular development, e.g. by calcium signalling[51] or mechanical contractility[52,53]. Robust strategies to initiate physiological function are likely to be broadly important for the progression of embryonic organogenesis.

References

1. DeHaan, R. L. The potassium-sensitivity of isolated embryonic heart cells increases with development. *Dev. Biol.* **23**, 226–240 (1970).
2. Arrenberg, A. B., Stainier, D. Y. R., Baier, H. & Huisken, J. Optogenetic Control of Cardiac Function. *Science* **330**, 971–974 (2010).
3. Bressan, M., Liu, G. & Mikawa, T. Early Mesodermal Cues Assign Avian Cardiac Pacemaker Fate Potential in a Tertiary Heart Field. *Science* **340**, 744–748 (2013).
4. Falcon, A. & Lefebvre, D. *Aristotle's Generation of Animals: A Critical Guide*. (Cambridge University Press, 2018).
5. Sabin, F. Studies on the origin of blood-vessels and of red blood-corpuscles as seen in the living blastoderm of chicks during the second day of incubation. *Contrib Embryol Carneg Inst* **9**, 214–262 (1920).
6. Patten, B. M. Initiation and early changes in the character of the heart beat in vertebrate embryos. *Physiol. Rev.* **29**, 31–47 (1949).
7. Van Mierop, L. Location of pacemaker in chick embryo heart at the time of initiation of heartbeat. *Am. J. Physiol.* **212**, 407–415 (1967).
8. Kamino, K., Hirota, A. & Fujii, S. Localization of pacemaking activity in early embryonic heart monitored using voltage-sensitive dye. *Nature* **290**, 595–597 (1981).
9. Hirota, A., Kamino, K., Komuro, H., Sakai, T. & Yada, T. Early events in development of electrical activity and contraction in embryonic rat heart assessed by optical recording. *J. Physiol.* **369**, 209–227 (1985).
10. Hirota, A., Kamino, K., Komuro, H. & Sakai, T. Mapping of early development of electrical activity in the embryonic chick heart using multiple-site optical recording. *J. Physiol.* **383**, 711–728 (1987).
11. Tyser, R. C. *et al.* Calcium handling precedes cardiac differentiation to initiate the first heartbeat. *eLife* **5**, e17113 (2016).
12. Panáková, D., Werdich, A. A. & MacRae, C. A. Wnt11 patterns a myocardial electrical gradient through regulation of the L-type Ca 2+ channel. *Nature* **466**, 874–878 (2010).
13. Entcheva, E. & Kay, M. W. Cardiac optogenetics: a decade of enlightenment. *Nat. Rev. Cardiol.* **18**, 349–367 (2021).
14. Dana, H. *et al.* High-performance calcium sensors for imaging activity in neuronal populations and microcompartments. *Nat. Methods* **16**, 649–657 (2019).

15. Werley, C. A., Chien, M.-P. & Cohen, A. E. Ultrawidefield microscope for high-speed fluorescence imaging and targeted optogenetic stimulation. *Biomed. Opt. Express* **8**, 5794–5813 (2017).
16. Dalangin, R. *et al.* Far-red fluorescent genetically encoded calcium ion indicators. *bioRxiv* 2020.11.12.380089 (2020) doi:10.1101/2020.11.12.380089.
17. Huang, C.-J., Tu, C.-T., Hsiao, C.-D., Hsieh, F.-J. & Tsai, H.-J. Germ-line transmission of a myocardium-specific GFP transgene reveals critical regulatory elements in the cardiac myosin light chain 2 promoter of zebrafish. *Dev. Dyn.* **228**, 30–40 (2003).
18. Zhou, Y. *et al.* Latent TGF-β binding protein 3 identifies a second heart field in zebrafish. *Nature* **474**, 645–648 (2011).
19. Izhikevich, E. M. *Dynamical systems in neuroscience*. (MIT press, 2007).
20. Hesse, J., Schleimer, J.-H., Maier, N., Schmitz, D. & Schreiber, S. Temperature elevations can induce switches to homoclinic action potentials that alter neural encoding and synchronization. *Nat. Commun.* **13**, 3934 (2022).
21. Meisel, C., Klaus, A., Kuehn, C. & Plenz, D. Critical Slowing Down Governs the Transition to Neuron Spiking. *PLOS Comput. Biol.* **11**, e1004097 (2015).
22. Salvi, J. D., Ó Maoiléidigh, D. & Hudspeth, A. J. Identification of Bifurcations from Observations of Noisy Biological Oscillators. *Biophys. J.* **111**, 798–812 (2016).
23. Morris, C. & Lecar, H. Voltage oscillations in the barnacle giant muscle fiber. *Biophys. J.* **35**, 193–213 (1981).
24. Kuznetsov, Y. A. *Elements of Applied Bifurcation Theory*. vol. 112 (Springer, 2004).
25. Galione, A. *et al.* Redundant Mechanisms of Calcium-Induced Calcium Release Underlying Calcium Waves During Fertilization of Sea Urchin Eggs. *Science* **261**, 348–352 (1993).
26. Collier, M. L., Ji, G., Wang, Y.-X. & Kotlikoff, M. I. Calcium-Induced Calcium Release in Smooth Muscle: Loose Coupling between the Action Potential and Calcium Release. *J. Gen. Physiol.* **115**, 653–662 (2000).
27. Abdelfattah, A. S. *et al.* Bright and photostable chemigenetic indicators for extended in vivo voltage imaging. *Science* **365**, 699–704 (2019).
28. Rottbauer, W. *et al.* Growth and Function of the Embryonic Heart Depend upon the Cardiac-Specific L-Type Calcium Channel α1 Subunit. *Dev. Cell* **1**, 265–275 (2001).
29. Hou, J. H., Kralj, J. M., Douglass, A. D., Engert, F. & Cohen, A. E. Simultaneous mapping of membrane voltage and calcium in zebrafish heart in vivo reveals chamber-specific developmental transitions in ionic currents. *Front. Physiol.* **5**, (2014).
30. Rapila, R., Korhonen, T. & Tavi, P. Excitation–Contraction Coupling of the Mouse Embryonic Cardiomyocyte. *J. Gen. Physiol.* **132**, 397–405 (2008).
31. Lakatta Edward G., Maltsev Victor A., & Vinogradova Tatiana M. A Coupled SYSTEM of Intracellular Ca2+ Clocks and Surface Membrane Voltage Clocks Controls the Timekeeping Mechanism of the Heart's Pacemaker. *Circ. Res.* **106**, 659–673 (2010).
32. Jou, C. J. *et al.* A Functional Assay for Sick Sinus Syndrome Genetic Variants. *Cell. Physiol. Biochem.* **42**, 2021–2029 (2017).
33. Shu, X. *et al.* Na,K-ATPase is essential for embryonic heart development in the zebrafish. *Development* **130**, 6165–6173 (2003).
34. Klapoetke, N. C. *et al.* Independent optical excitation of distinct neural populations. *Nat. Methods* **11**, 338–346 (2014).
35. Leybaert, L. & Sanderson, M. J. Intercellular Ca2+ waves: Mechanisms and function. *Physiol. Rev.* **92**, 1359–1392 (2012).
36. Staudt, D. & Stainier, D. Uncovering the molecular and cellular mechanisms of heart development using the zebrafish. *Annu. Rev. Genet.* **46**, 397–418 (2012).
37. Ren, J. *et al.* Canonical Wnt5b Signaling Directs Outlying Nkx2.5+ Mesoderm into Pacemaker Cardiomyocytes. *Dev. Cell* **50**, 729-743.e5 (2019).

38. Rohr, S., Otten, C. & Abdelilah-Seyfried, S. Asymmetric Involution of the Myocardial Field Drives Heart Tube Formation in Zebrafish. *Circ. Res.* **102**, e12–e19 (2008).
39. Smith, K. A. *et al.* Rotation and Asymmetric Development of the Zebrafish Heart Requires Directed Migration of Cardiac Progenitor Cells. *Dev. Cell* **14**, 287–297 (2008).
40. Govorunova, E. G., Sineshchekov, O. A., Janz, R., Liu, X. & Spudich, J. L. Natural light-gated anion channels: A family of microbial rhodopsins for advanced optogenetics. *Science* **349**, 647–650 (2015).
41. Vassalle, M. The relationship among cardiac pacemakers. Overdrive suppression. *Circ. Res.* **41**, 269–277 (1977).
42. Cavanaugh, M. W. Pulsation, migration and division in dissociated chick embryo heart cells in vitro. *J. Exp. Zool.* **128**, 573–589 (1955).
43. Chen, J. N. *et al.* Mutations affecting the cardiovascular system and other internal organs in zebrafish. *Development* **123**, 293–302 (1996).
44. Tsimring, L. S. Noise in biology. *Rep. Prog. Phys.* **77**, 026601 (2014).
45. Dai, L., Vorselen, D., Korolev, K. S. & Gore, J. Generic Indicators for Loss of Resilience Before a Tipping Point Leading to Population Collapse. *Science* **336**, 1175–1177 (2012).
46. Horikawa, K., Ishimatsu, K., Yoshimoto, E., Kondo, S. & Takeda, H. Noise-resistant and synchronized oscillation of the segmentation clock. *Nature* **441**, 719–723 (2006).
47. Tsai, T. Y.-C. *et al.* An adhesion code ensures robust pattern formation during tissue morphogenesis. *Science* **370**, 113–116 (2020).
48. Hänggi, P. Stochastic Resonance in Biology: How Noise Can Enhance Detection of Weak Signals and Help Improve Biological Information Processing. *ChemPhysChem* **3**, 285–290 (2002).
49. Brunel, N. & Latham, P. E. Firing Rate of the Noisy Quadratic Integrate-and-Fire Neuron. *Neural Comput.* **15**, 2281–2306 (2003).
50. Sehnert, A. J. *et al.* Cardiac troponin T is essential in sarcomere assembly and cardiac contractility. *Nat. Genet.* **31**, 106–110 (2002).
51. Andersen, N. D. *et al.* Calcium signaling regulates ventricular hypertrophy during development independent of contraction or blood flow. *J. Mol. Cell. Cardiol.* **80**, 1–9 (2015).
52. Zhu, R. *et al.* Physical developmental cues for the maturation of human pluripotent stem cell-derived cardiomyocytes. *Stem Cell Res. Ther.* **5**, 117 (2014).
53. North, T. E. *et al.* Hematopoietic Stem Cell Development Is Dependent on Blood Flow. *Cell* **137**, 736–748 (2009).

Acknowledgments: This work was supported by the Howard Hughes Medical Institute (A.E.C.), a Vannevar Bush Faculty Fellowship (AEC) and the Harvard Medical School John S. Ladue Fellowship in cardiovascular medicine (B.Z.J.). We thank C.E. and C.G. Burns for providing *TgBAC(-36Nkx2.5:ZsYellow)* transgenic fish; N. Chi for providing *Tg(7xTCF-Xla.Siam:nlsmCherry)*; I.C. Scott for providing the zACNE20 enhancer element; Y. Shen and R.A. Campbell for providing FR-GECO1c plasmid; L.D. Lavis for providing JaneliaFluor 608 dye; H.C. Davis and F.P. Brooks for developing microscope control software; J. Miller-Henderson, K. Hurley, and A.R. Murphy for fish husbandry; and members of the Megason lab for assistance with fish husbandry.

Author contributions: A.E.C, B.Z.J., and S.G.M. conceived the project and designed experiments. B.Z.J. performed all experiments, data analysis, and numerical modeling. B.Z.J. constructed molecular tools and transgenic fish lines. Y.Q., J.D.W.C., and B.Z.J. performed optical engineering of microscopes. B.Z.J., A.E.C. and S.G.M. wrote the manuscript with input from all authors. A.E.C. and S.G.M. supervised the project.

Competing interests: The authors declare no competing interests.

Additional information: Supplementary Information is available for this paper. Correspondence and requests for materials should be addressed to Adam E. Cohen (cohen@chemistry.harvard.edu) or Sean G. Megason (megason@hms.harvard.edu). Reprints and permissions information is available at www.nature.com/reprints.

Figures

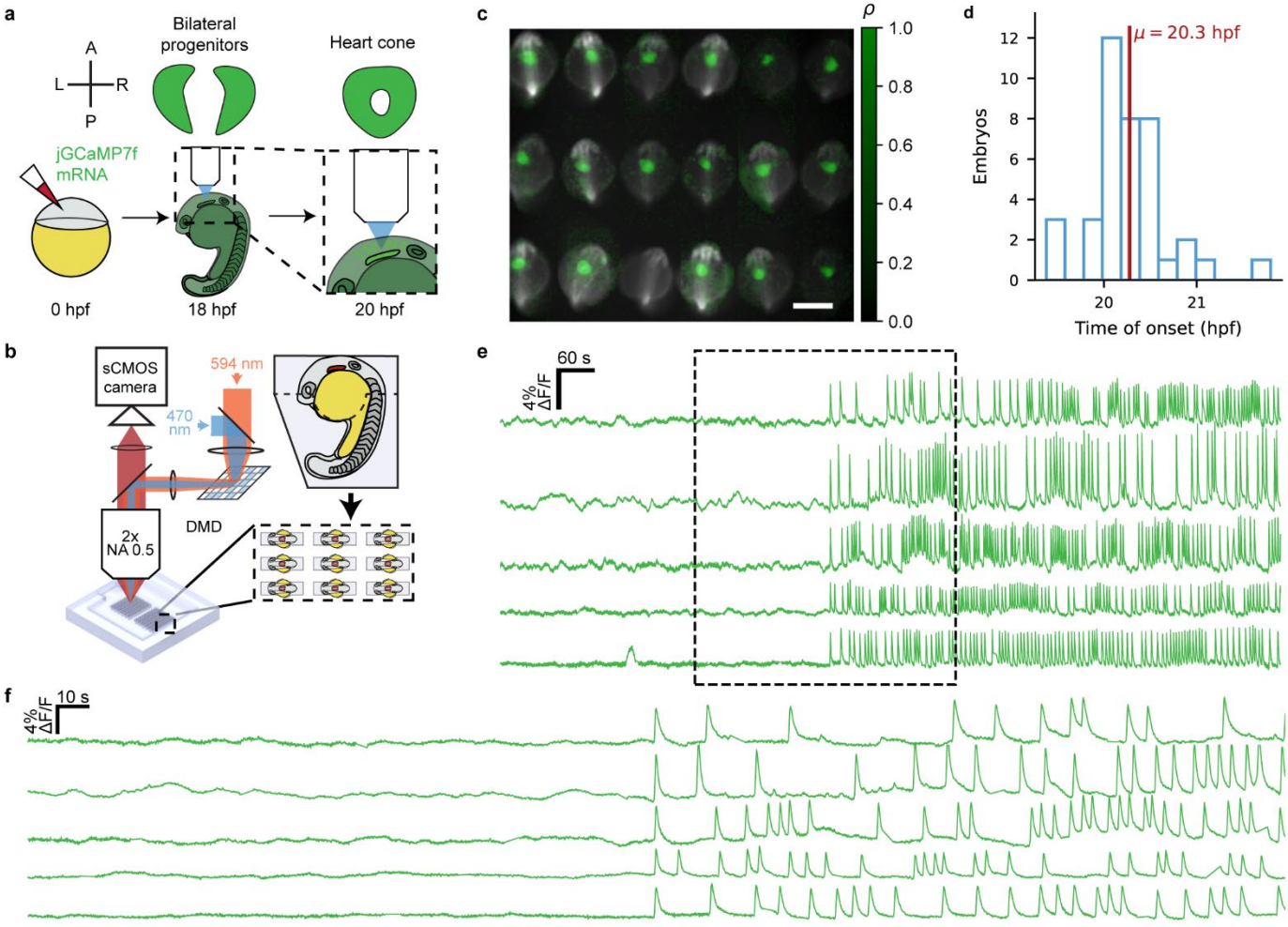

Fig. 1: Multiplexed time-lapse calcium imaging captures the first heartbeats of zebrafish embryos. a, Injection of mRNA encoding jGCaMP7f for whole-embryo Ca^{2+} imaging during zebrafish heart cone formation. **b**, Low-magnification microscopy platform and array mount for multiplexed live imaging and all-optical electrophysiology. **c,** representative Pearson correlation (green) of individual pixel time traces to putative cardiac activity (3/3 experiments). Activity maps are overlaid on grayscale images of baseline fluorescence. Scale bar, 500 µm. **d**, Histogram of time of onset of the first cardiac calcium spike (n = 39 embryos, 3 experiments). **e**, jGCaMP7f ΔF/F measurements of representative hearts aligned by the first calcium spike. **f**, Zoomed-in traces from **e**.

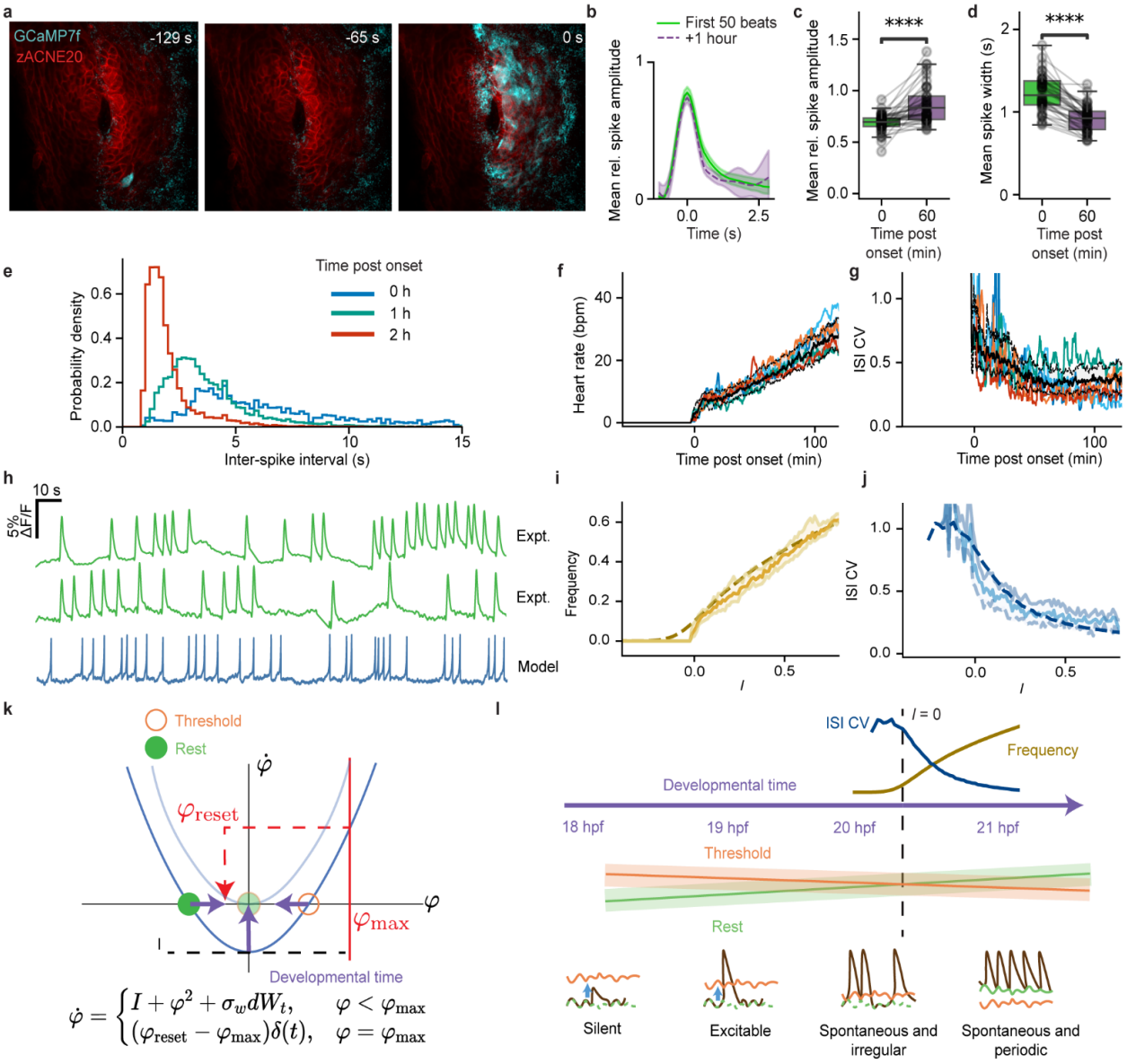

Fig. 2: The heartbeat undergoes coordinated initiation via a noisy SNIC bifurcation. a, Single-cell calcium transients followed by a large-scale coherent event at t = 0 (3/3 embryos, quantified in Extended Data Fig. 3). Scale bar, 50 µm. **b**, Spike-triggered average waveform over 50 spikes for individual embryos at onset and 1 hour post onset (hpo). Error bar is standard deviation over spikes at each time sample. **c**,**d**, aAverage transient amplitude (**c**) and spike width (**d**) over 50 beats starting from the first beat and starting from 1 h later. Circles linked by lines represent values at different timepoints for individual embryos. Boxplots represent interquartile range (IQR; 25th, 50th, 75th percentile) with whiskers representing 1.5x IQR. **e**, Population distribution of inter-spike intervals (ISIs) in selected 10-minute windows relative to the first heartbeat. **f**, **g**, Beat rate (**f**) and ISI coefficient of variation (ISI CV; **g**) aligned to the first heartbeat. Black line: median; dotted lines and shading: interquartile range; colored lines: representative individual traces. **h**, Example traces of the first calcium spikes (green; top trace is the middle trace

from Fig. **1f**, reproduced) and QIF-generated simulation (blue). **i,j** Experimental frequency and CV jointly fit to the quadratic integrate-and-fire (QIF) model (dashed line, Supplementary Information, Extended Data Fig. 4) with linear scalings of drive current to developmental time. Shaded region is ±95% CI. **b** – **j** Same individuals as Fig. **1d**, n = 39 embryos, 3 experiments. **k**, Phase portrait of the QIF model as it undergoes a SNIC bifurcation (Supplementary Information).

l, Schematic describing emergence of spiking regimes in the early heartbeat driven by a noisy phase transition. Statistical test values: T = 27.0, p = 4.07e-7, **** (**c**); T = 0.0, p = 5.26e-8, **** (**d**). Two-sided Wilcoxon signed-rank test.

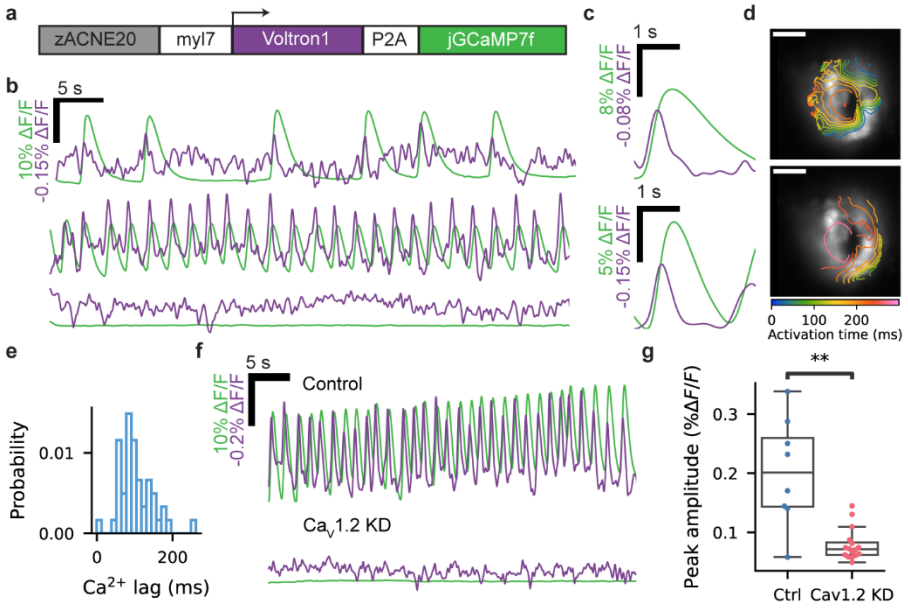

Fig. 3: Membrane potential is coupled to calcium dynamics in the first heartbeats. a, Genetic construct for simultaneous imaging of calcium and membrane voltage (V_{mem}). **b**, Calcium (green) and V_{mem} (purple) dynamics. Top: early heart primordium (6 bpm, estimated 15 – 30 mpo), middle: more mature specimen (25 bpm, estimated 110 mpo), bottom: specimen before onset of calcium dynamics. **c**, Spike-triggered averages (STAs) of the top two traces in **b**. **d**, Isochronal lines of V_{mem} action potentials corresponding to the 6 bpm and 25 bpm recordings in **b** and **c**. Grayscale image, absolute value of the first spatial PC of the calcium recording. Scale bars, 50 µm**. e**, Distribution of lags between voltage and calcium action potential upstrokes (Methods). **a - e**, 40 recordings from 36 embryos in one experiment. Data from **f** and **g** included in analysis. **f,** Dual recordings of V_{mem} and calcium for control and $Ca_V1.2$ knockdown (*cacna1c* morpholino) embryos at 22-23 hpf. **g,** Comparison of amplitude of electrical events in control and knockdown embryos. Boxplot represents interquartile range (IQR; 25th, 50th, 75th percentile) with whiskers representing 1.5x IQR. Control, n = 7 embryos; KD, n = 15 embryos. Statistical test values: U = 1.52e6, p ~ 0 **** (**g**). Mann-Whitney-Wilcoxon two-sided test.

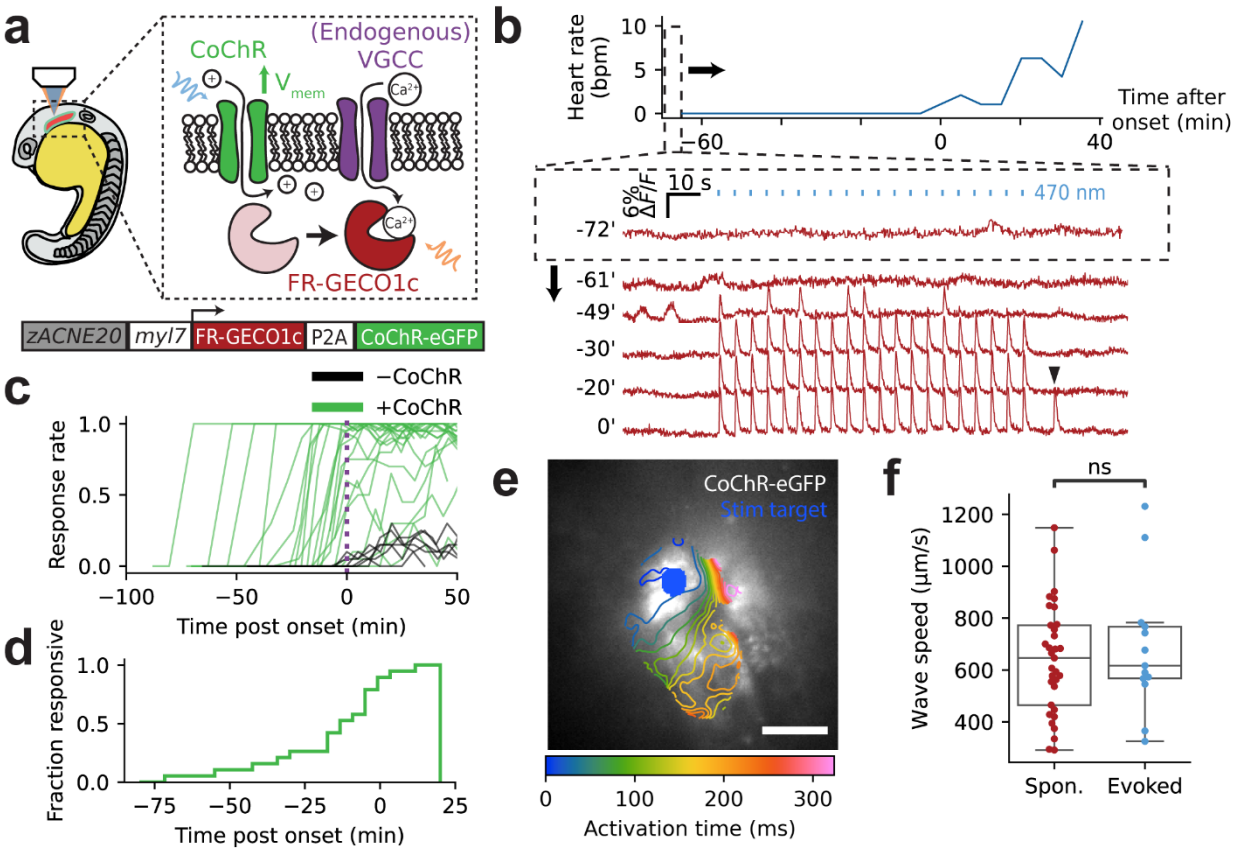

Fig. 4: The heart primordium is excitable and electrically coupled before the first heartbeat. **a**, Genetic construct for simultaneous optogenetic stimulation and calcium imaging. **b**, Repeated testing of response to optogenetic stimulation in silent hearts. Black triangle indicates the first detected spontaneous beat. **c**, Response rate to optogenetic stimuli in individual embryos. Response rate for embryos not expressing CoChR was a result of spontaneous transients randomly aligning with blue light pulses. **d**, Fraction of the population displaying a greater than 50% response rate. **c**, **d**, n = 5 embryos -CoChR, n = 21 embryos +CoChR, two experiments. **e,** Activation map for triggered averages of calcium elevation evoked by localized stimulus before heartbeat initiation. Scale bar, 50 µm. **f**, Wave propagation speeds for early spontaneous activity and activity evoked before heartbeat initiation. Evoked, thirteen 45-second recordings, n = 7 embryos, 2 experiments. Spontaneous, ninety 30-second recordings, n = 12 embryos, 3 experiments. Circles represent individual recordings. Boxplot represents interquartile range (IQR; 25th, 50th, 75th percentile) with whiskers representing 1.5x IQR. Statistical test values: t = 0.60, p = 0.55, n.s. Two-tailed unpaired t-test.

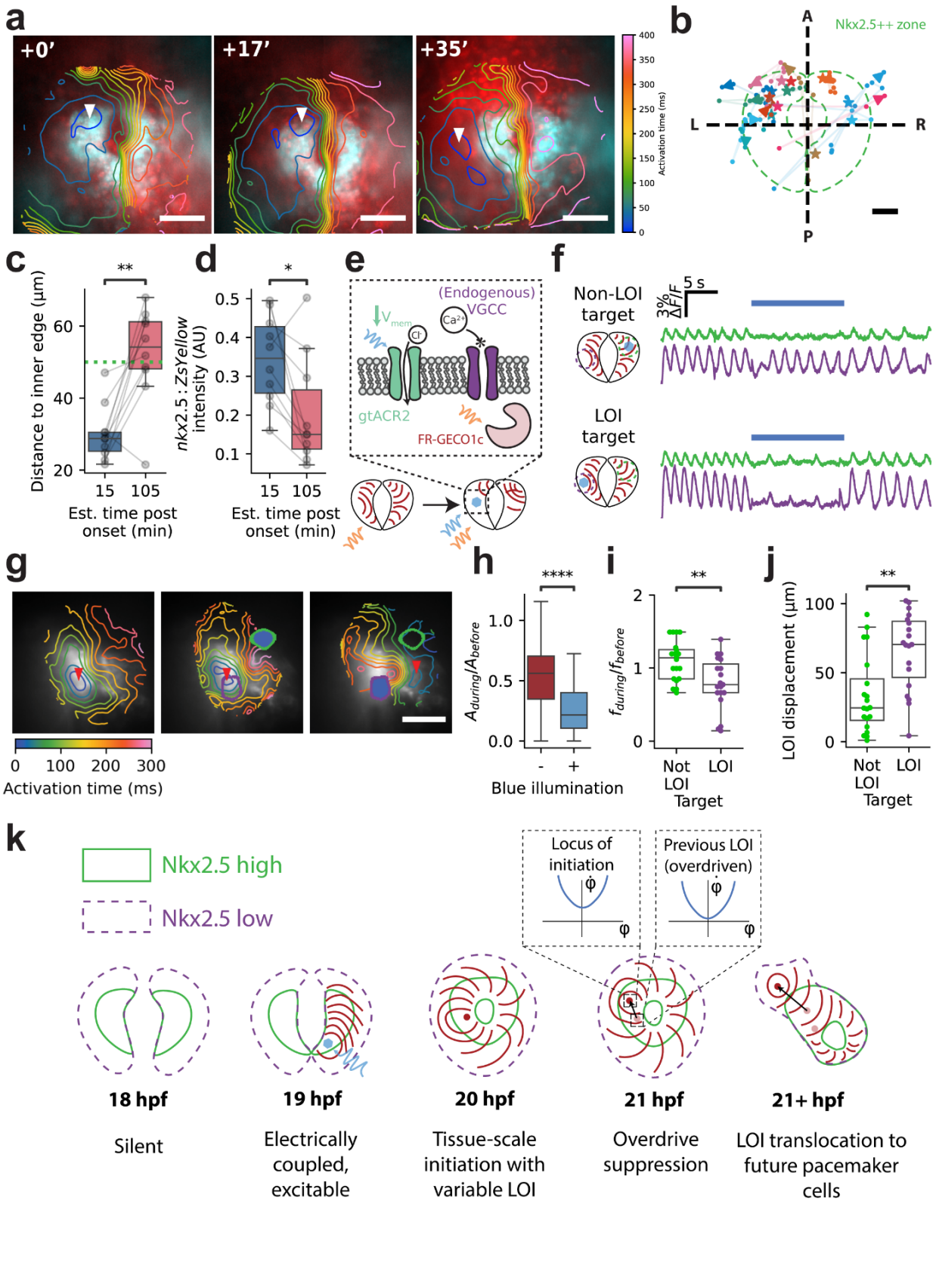
a
+0'
+17'
+35'
400
350
300
250
200
150
100
50
0
Activation time (ms)
b
A
P
L
R
Nkx2.5++ zone
c
**
Distance to inner edge (µm)
60
40
20
15
105
Est. time post onset (min)
d
*
nkx2.5:ZsYellow intensity (AU)
0.5
0.4
0.3
0.2
0.1
15
105
Est. time post onset (min)
e
(Endogenous) VGCC
V_{mem}
Cl^-
Ca^{2+}
gtACR2
FR-GECO1c
f
Non-LOI target
LOI target
3% ΔF/F
5 s
g
0
100
200
300
Activation time (ms)
h
****
A_{during}/A_{before}
1.0
0.5
0.0
-
+
Blue illumination
i
**
f_{during}/f_{before}
2
1
0
Not LOI Target
LOI
j
**
LOI displacement (µm)
100
50
0
Not LOI Target
LOI
k
Nkx2.5 high
Nkx2.5 low
Locus of initiation
Previous LOI (overdriven)
φ
18 hpf
Silent
19 hpf
Electrically coupled, excitable
20 hpf
Tissue-scale initiation with variable LOI
21 hpf
Overdrive suppression
21+ hpf
LOI translocation to future pacemaker cells

Fig. 5: Wave geometry of the early heartbeat is set by competition between spontaneously firing cells. a, Activation maps of spontaneous activity in a representative embryo, showing drift of the locus of initiation over time (LOI; white/red triangle in all panels). Scale bar, 50 μm. Cyan: nkx2.5:ZsYellow, Red: TCF:nls-mCherry. **b**, LOI trajectories for individual embryos. Star indicates initial measurement, arrowhead indicates final measurement. Imaging intervals varied from 5.5 to 30.5 minutes (mean 14.6 minutes). Green dashed line indicates the approximate extent of the (strongly) Nkx2.5++ region. A: anterior, P: posterior, L: left, R: right. Scale bar, 25 μm. **c**, distance from inner edge of Nkx2.5++ region, and **d**, relative nkx2.5:ZsYellow intensity of the LOI as heartbeat maturation progresses. **b** – **d**, n = 12 embryos, 3 experiments. **e**, Schematic of optogenetic silencing. VGCC = voltage-gated calcium channel. **f-f'**, Example ΔF/F traces showing localized silencing. Purple: spontaneous LOI; green: non-LOI region. Blue circle: silencing target. **g-g''**, Activation maps of endogenous activity (**g**) and associated with **f (g')** and **f' (g'')**. Scale bar, 50 μm. **h**, Relative calcium transient amplitude (A) in the silenced ROI (+; median 0.216, IQR 0.106 – 0.401) and in distal locations (-; median 0.562, IQR 0.348 – 0.705). **i,j**Relative heart rate (f) (**i**) and LOI displacement (**j**) as a function of optogenetic silencing location. **h** – **j**, 39 observations, 13 embryos, 5 experiments. **k**, Schematic describing spatial patterning of the early heartbeat. All boxplots represent IQR with whiskers representing 1.5x IQR. Statistical test values: t = -4.55, p = 1.381e-3, ** (**c**); W = 5, p = 1.95e-2, * (**d**); U = 4350, p = 1.51e-8, **** (**h**); t = 2.96, p = 5.34e-3, ** (**i**); U = 300, p = 2.0e-3, ** (**j**). Two-tailed paired t-test (**c**), two-sided Wilcoxon signed-rank test (**d**), Mann-Whitney-Wilcoxon two-sided test (**h**, **j**), two-tailed unpaired t-test (**i**).

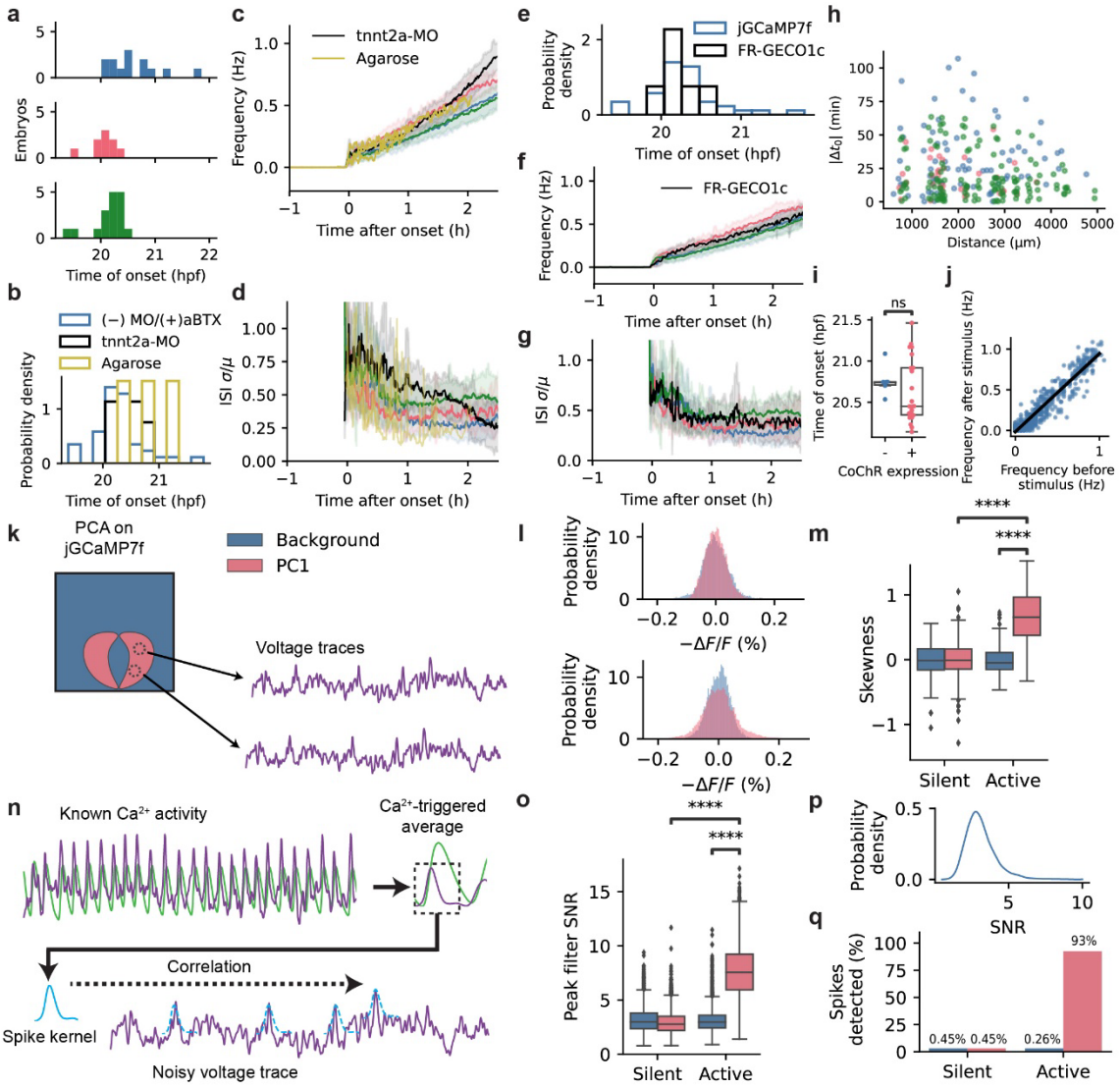

Extended Data Fig. 1: Technical validations of experimental approaches. a, Histograms of onset time for experimental replicates. **b,** Comparison of time of onset for alpha-bungarotoxin (aBTX) mRNA-injected embryos (n = 40), tnnt2a morphants (n = 12), and agarose-encased embryos (n = 3) respectively. **c,d,** Comparison of frequency (**c**) and inter-spike interval coefficient of variation (ISI CV, **d**) as a function of time after the first beat. aBTX mRNA-injected replicates colored corresponding to (**a**). **e,** Time of onset for jGCaMP7f-expressing embryos (n = 40) and FR-GECO1c-expressing embryos (n = 6). **f,g,** Comparison of frequency (**f**) and ISI CV (**g**) for jGCaMP7f and FR-GECO1c-expressing embryos. **h,** Difference in time of onset as a function of distance between all pairwise combinations of embryos in the experiments in (**a**). There was negligible correlation (r = 0.04, -0.05, -0.18 for each replicate, respectively), confirming absence of chemical or mechanical coupling between embryos. **i,** Time of onset for embryos +/- CoChR expression and exposed to pulsed blue light for the optogenetic stimulus program in Fig. 4. **j,** Spontaneous beat rate was unchanged before vs. after optogenetic stimulation protocol. **k**, Method of extracting voltage signals from *Tg(z20m:Voltron1-P2A-jGCaMP7f)* heart primordia. **l**,

Probability distributions of Voltron1 -ΔF/F in background (blue) and jGCaMP7f principal component 1 (PC1, red) regions, before (top) and after (bottom) initiation of calcium transients. **m**, Skewness of Voltron1 -ΔF/F distribution before (silent) and after (active) initiation of calcium transients. Positive skewness indicates presence of upwards spikes. **n**, Pipeline for performing matched filter analysis (Methods). **o**, Peak matched filter signal-to-noise ratio. **p**, Gaussian kernel density estimate of candidate spike SNR distribution for background regions. **q**, Fraction of candidate spike events with SNR greater than the 95th percentile of **p**. Candidate spike events were identified by performing peak detection on the jGCaMP7f recordings. .**a – h**, Three replicates of jGCaMP7f and aBTX mRNA-injected embryos at n = 13, n = 9, n = 18 animals respectively, tnnt2a morpholino at n = 12 animals, agarose-encased embryos at n = 3 animals, 1 experiment. FR-GECO1c and aBTX mRNA-injected embryos at n = 6 animals. **i – j**, n = 6 control animals and n = 21 CoChR-expressing animals over 2 experiments. **k–q**, 18 recordings with detectable calcium transients, 22 recordings without, across 36 embryos in one experiment. **m,o**, 10408 traces from regions of interest. **q**, 597 putative spikes analyzed (377 in "active" recordings, 220 in "silent" recordings). Boxplots represent interquartile range (IQR; 25th, 50th, 75th percentile) with whiskers representing 1.5x IQR. Statistical test values: (**i**) $U = 45$, $p = 0.26$, Mann-Whitney-Wilcoxon two-sided test; (**j**) linear regression $y = 0.96x - 0.018$, $r = 0.959$, $p = 0$, Wald Test; (**m**), **(o),** $p = 0$ in all comparisons shown, Mann-Whitney-Wilcoxon two-sided test with Benjamini-Hochberg correction.

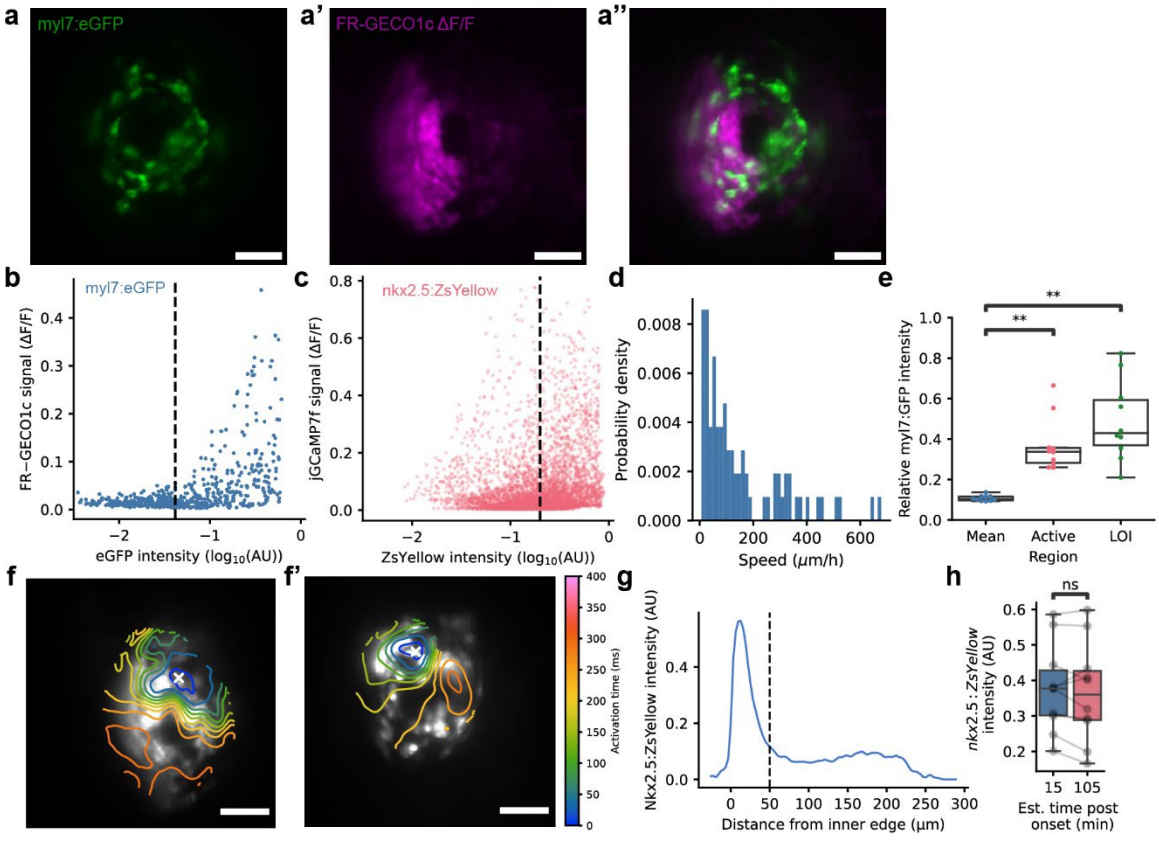

Extended Data Fig. 2: Calcium dynamics colocalize with genetic markers of developing cardiomyocytes. a, Tg(*myl7:eGFP*) expression in a 20 – 21 hpf embryo. **a'**, Peak ΔF/F of

ubiquitously expressed FR-GECO1c during a spike-triggered average video (Methods). **a''**, Merge. Scale bars 50 μm. **b**, Relationship between peak FR-GECO1c ΔF/F and *myl7:eGFP* intensity for tiled regions of interest (Methods). **c**, Relationship between peak jGCaMP7f ΔF/F and *nkx2.5:ZsYellow* intensity for tiled regions of interest. Same embryos as in Fig. 5a – d. **b**, **c**, dashed line indicates 50th percentile of fluorophor intensity. **d**, Distribution of LOI motion speed. **e**, Relative GFP intensity in Ca^{2+} active regions and LOIs, compared to image mean. n = 10 embryos, 15 – 45 minutes post onset. **f – f'**, Example activation maps of ubiquitously expressed FR-GECO1c in Tg(*myl7:eGFP*) embryos. GFP in grayscale. Scale bars 50 μm. **g**, Relative *nkx2.5:ZsYellow* intensity as a function of distance from the inner edge of the heart cone. A region approximately < 50 μm from the inner edge had stronger expression than more distal cells. **h**, Relative nkx2.5:ZsYellow intensity at the location of the 15 mpo LOI did not change between 15 mpo and 105 mpo, suggesting stable nkx2.5 expression in this region. **a, b, e, f,** n = 10 embryos over one experiment, 15 – 45 minutes post onset. **c, h,** Data from Fig. 5a – d (n = 12 embryos, 3 experiments). **g,** Data from Extended Data Fig. 4e – f. Boxplots represent interquartile range (IQR; 25th, 50th, 75th percentile) with whiskers representing 1.5x IQR. Statistical test values: (**e**) mean vs. active, T = 0, p = 1.953e-3, **, mean vs. LOI T = 0, p = 1.953e-3, **; (**h**), T = 17, p = 0.32. Two-sided Wilcoxon signed-rank test with Benjamini-Hochberg correction.

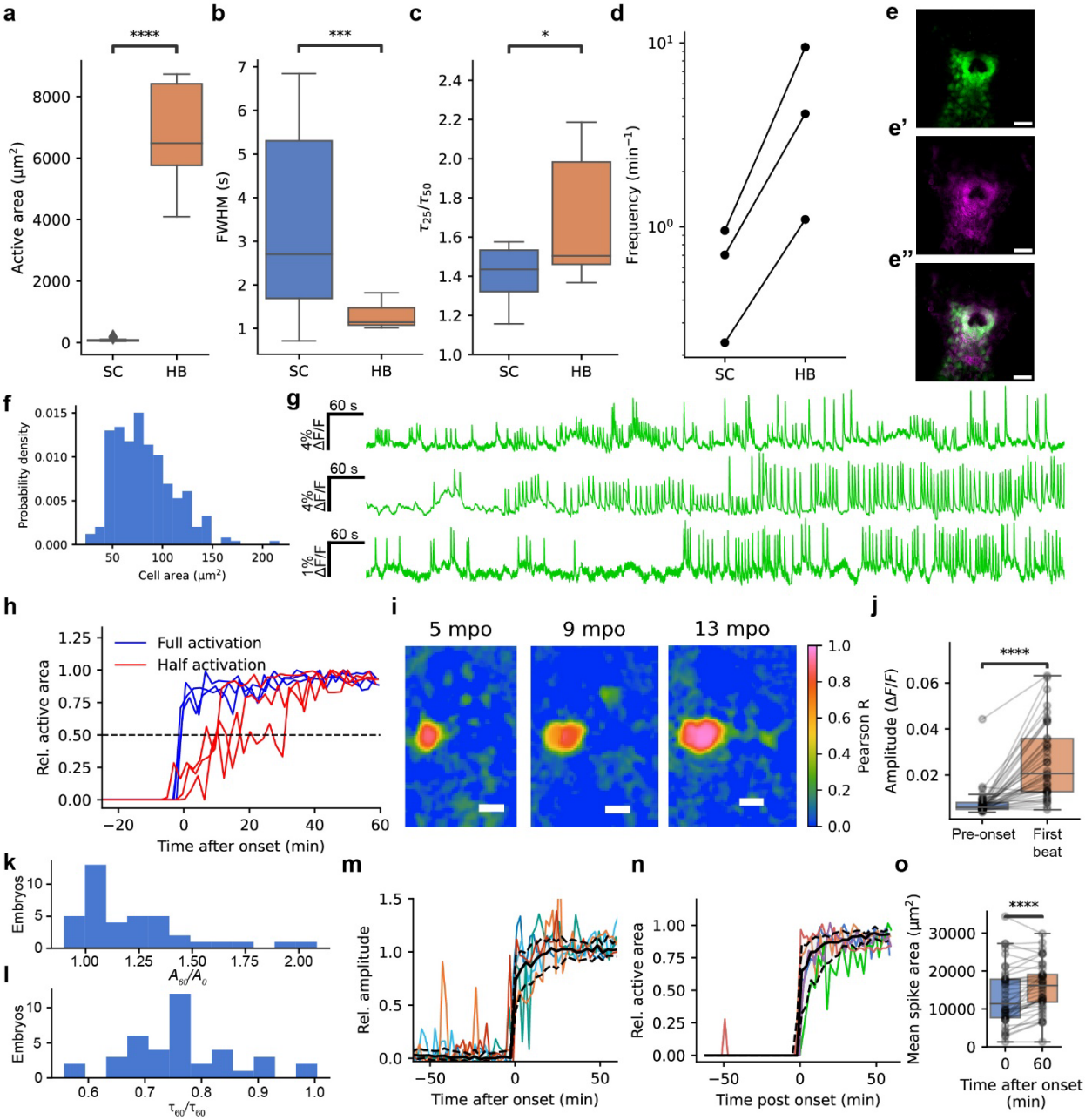

Extended Data Fig. 3: Spatiotemporal structure of the transition from silent to beating. a, Active area of single-cell (SC) transients (74 ± 32 µm^2) was much lower than that of the first heartbeats (HB, 7000 ± 1400 µm^2). **b**, Single-cell transients were longer lived (3.4 ± 2.1 s) than the first heartbeats (1.3 ± 0.2 s). FWHM: full-width half-maximum. **c**, Single-cell transients had a longer plateau phase than the first heartbeats, as quantified by the ratio of peak width at 25% (τ_{25}) and 50% (τ_{50}) of maximum height. **d**, Single-cell transients were rare (0.2 – 0.7 per minute) compared to the first heartbeats (1 – 9.5 per minute). **a – d**, Data from 19 single-cell transients and 50 beats across *n* = 3 embryos over 3 experiments. **e – e''**, Maximum intensity projection fluorescence images of 21-somite stage Tg(*-36nkx2.5:ZsYellow; zACNE20:2xLyn-mCherry*) heart cone (5/5 embryos over 1 experiment). **e**, *nkx2.5:ZsYellow*. **e'**, *zACNE20:2xLyn-mCherry*. **e''**,

Merge. **f,** Cell area distribution. Mean area 82 μm^2 (± 29 μm^2 SD). n = 5 embryos, 254 cells, over 1 experiment. Scale bars 50 μm. Mean ± SD for all values in caption. **g**, jGCaMP7f fluorescence starting from 2 minutes after the first heartbeat in embryos with spontaneous initiation in half the heart. The traces were averaged over the whole heart, so traces that engaged half the heart had approximately half the apparent amplitude of traces that engaged the whole heart. **h**, Relative active areas of the traces in **g** compared to representative traces of embryos with full-tissue initiation. Area was averaged in a 2-minute sliding window. **i,** Pearson correlation between fluorescence dynamics of individual pixels and the mean segmented heartbeat jGCaMP7f activity at different timepoints. The sharp boundary in the 9 minutes post onset (mpo) image is due to roughly half the heart being engaged in some but not all beats. Same experiments as in Figure 1. Scale bars 100 μm. **j**, Amplitude of the first detected calcium transient compared to maximum fluctuation from mean in the previous 2 minutes. **k**, Ratio of calcium transient amplitudes (ΔF/F) 60 minutes post onset (mpo, A_{60}) and 0 mpo (A_0). **l**, Ratio of transient widths (full-width half-maximum) 60 minutes mpo (τ_{60}) and 0 mpo (τ_0). **m**, Amplitude of calcium transients as a function of time, aligned relative to first beat and normalized relative to initial beats. **n**, Active area of calcium transients as a function of time, aligned relative to first beat and normalized relative to initial beats (Methods). **m,n**, Colored lines show representative single-embryo traces. Black line shows median. Shading and dashed lines show interquartile range. **o**, Calcium spike area increased from 13490 ± 7730 μm^2 at 0 mpo to 15840 ± 6400 μm^2 at 60 mpo. **j – o**, n = 39 embryos across 3 experiments, same individuals as Figures 1-2. Boxplots represent interquartile range (IQR; 25th, 50th, 75th percentile) with whiskers representing 1.5x IQR. Statistical test values: (**a**) Two-sided Mann-Whitney-Wilcoxon test, p=6.5e-11, ****; (**b**) Two-sided Mann-Whitney-Wilcoxon test, p=1.3e-4, ***; (**c**) Two-sided Mann-Whitney-Wilcoxon test, p=0.015, *; (**j**) two-sided Wilcoxon signed-rank test, p = 1.23e-7, ****; (**o**) two-sided paired t-test, p = 5.4e-5, ****.

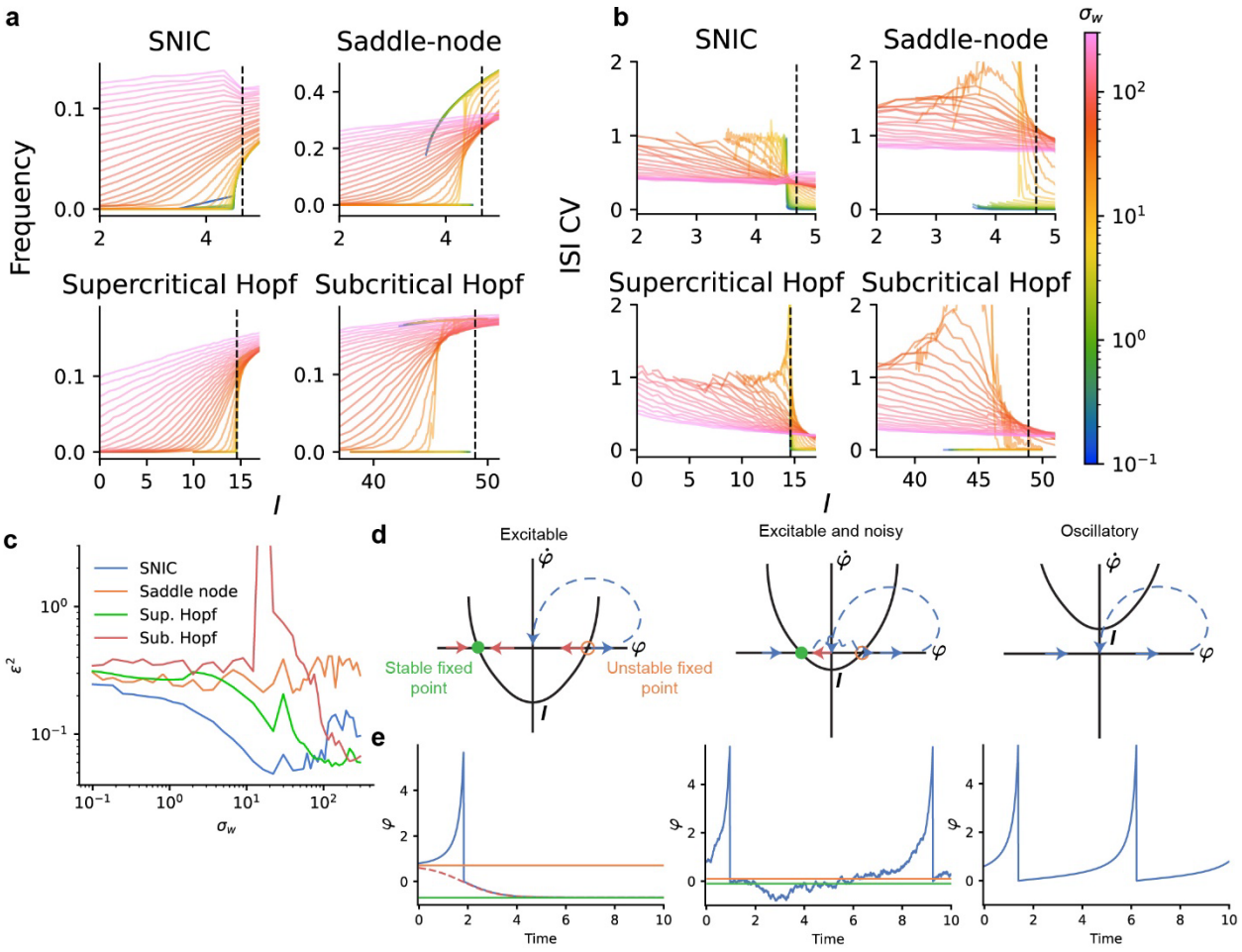

Extended Data Figure 4: Classification of the bifurcation class of heartbeat initiation. a, Mean frequency and **b**, inter-spike interval (ISI) coefficient of variation (CV) in simulated Morris-Lecar oscillators as a function of input current *I* and noise σ_w. Parameters given in Supplementary Table 2, were selected to drive each of the four types of co-dimension 1 bifurcation. **c**, Squared error (Supplementary Text) of experimental fits to each bifurcation at different values of σ_w. **d,** Spiking regimes across the SNIC bifurcation of the noisy quadratic integrate-and-fire (QIF) model (Supplementary Information Equation 2), shown by $\dot{\varphi}$ as a function of φ. **e**, Simulated example traces for each spiking regime.

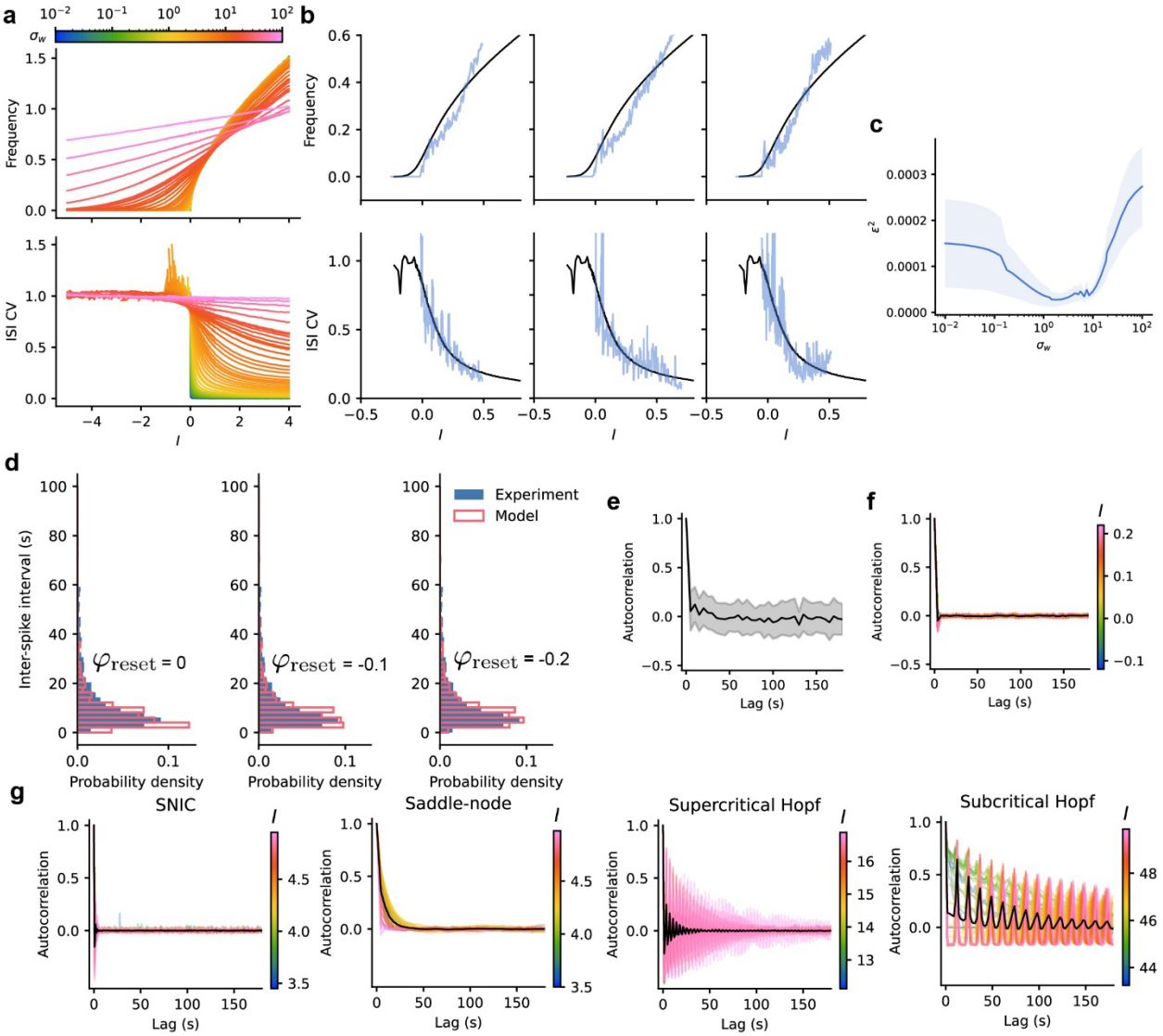

Extended Data Figure 5: A noisy quadratic integrate-and-fire model captures the experimental statistics of the first heartbeats. a, Simulated frequency and ISI CV for different values of noise σ_w. **b**, Example fits (top: frequency, bottom: ISI CV) of individual embryo data (blue) to simulation (black) with choices of σ_w which minimized squared error. **c**, Mean squared error of fits of simulated spike statistics to data as a function of σ_w ($n = 39$ embryos). **d**, Histograms of experimental and QIF-generated ISIs for the first 20 heartbeats, using different φ_{reset} values. Decreasing φ_{reset} modeled an increasing refractory period, and corrected the overrepresentation of short ISIs in the model relative to the data. **e**, Experimental autocorrelation of instantaneous frequency averaged over the first 50 heartbeats. **f**, Autocorrelation of instantaneous frequency in the QIF model with experimentally fitted σ_w and varying values of I. **g**, Autocorrelation of instantaneous frequency in the four bifurcation classes of the Morris-Lecar model, calculated using experimentally fitted σ_w and varying values of I.

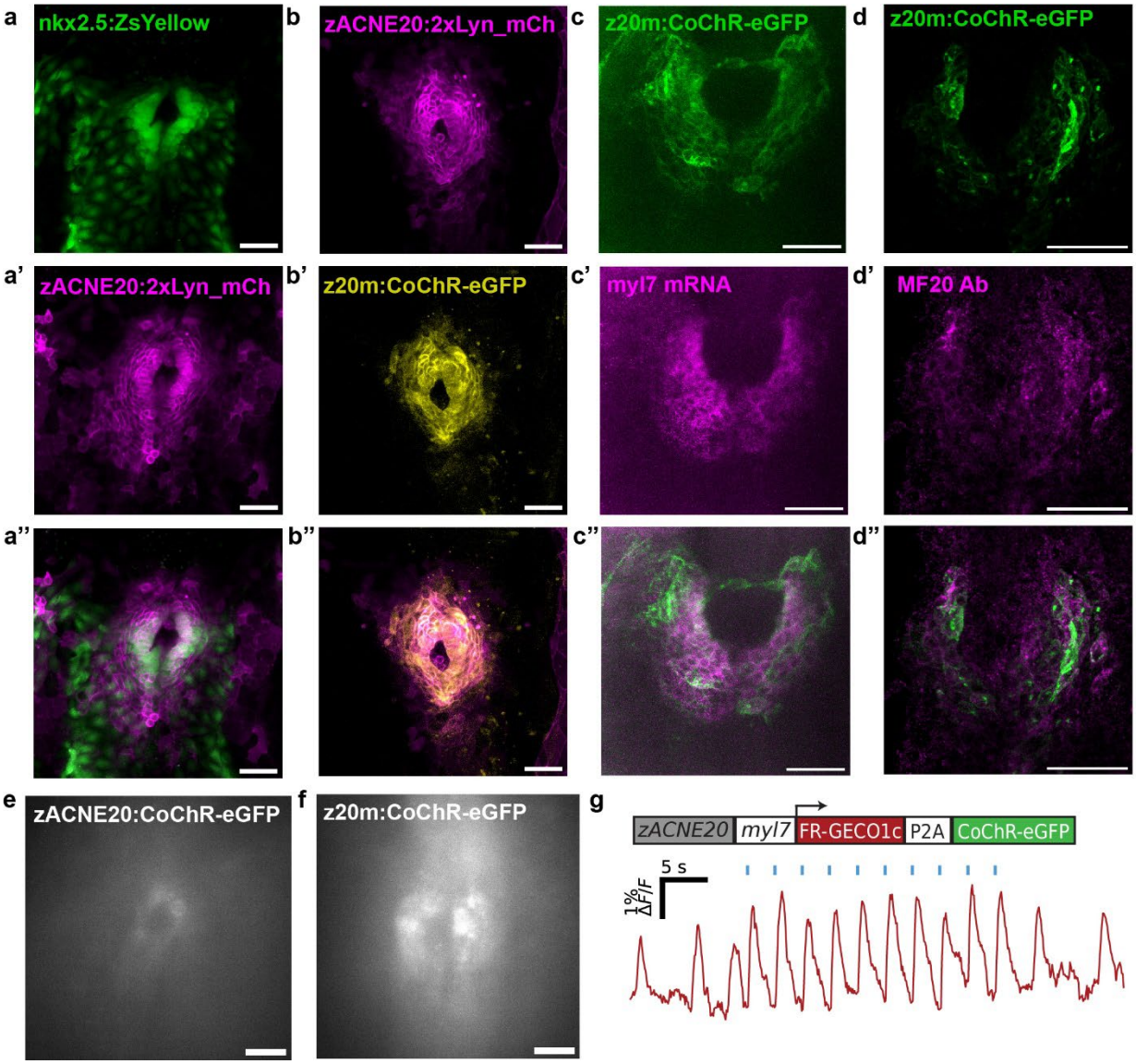

Extended Data Figure 6: Expression patterns of *zACNE20* and *zACNE20-myl7* (*z20m*) promoters in the early heart. a-a", Heart primordium in a 20-somite stage (ss) Tg(-36*nkx2.5:ZsYellow;zACNE20:2xLyn_mCherry*) embryo (5/5 embryos). **b-b"**, Heart cone in a 22 ss stage Tg(*zACNE20:2xLyn_mCherry; zACNE20-myl7: FRGECO1c-P2A-CoChR-eGFP*) embryo (6/6 embryos). **c-c"**, Heart primordium in an 18 – 19ss *Tg(z20m:FRGECO1c-P2A-CoChR-eGFP)* embryo stained for *myl7* using HCR-FISH (9/9 embryos). **d-d"**, Heart primordium in an 16 – 18ss *Tg(z20m:FRGECO1c-P2A-CoChR-eGFP)* embryo immunostained using MF20 antibody (6/6 embryos over 3 experiments). **a – d**, All images are confocal maximum intensity projections. **e**, **f**, *z20m* produces stronger expression than *zACNE20* at the same stage. Widefield images at 20-21 ss. **g**, example calcium recording and optogenetic stimulus in *zACNE20-myl7: FRGECO1c-P2A-CoChR-eGFP* at ~21 – 22 hpf (without additional mRNA). All scale bars 50 μm.

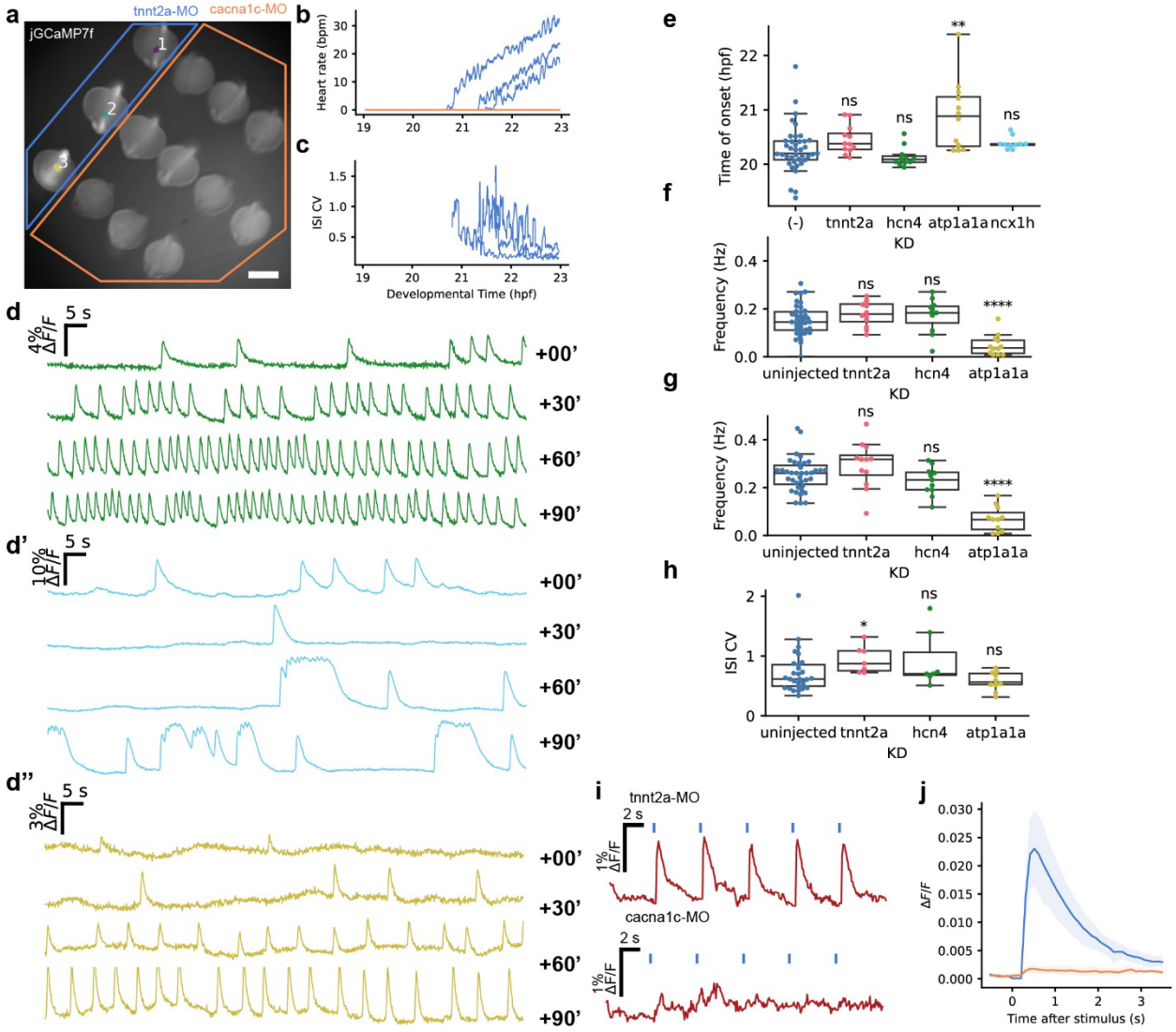

Extended Data Figure 7: The L-type calcium channel is required for excitability and initiation of spontaneous activity. a, Automatic segmentation (Methods) located heartbeats in control embryos but not in embryos injected with the *cacna1c* morpholino. *tnnt2a* KD, *n* = 3 embryos; *cacna1c* KD, *n* = 10 embryos. All embryos were injected with jGCaMP7f mRNA. Scale bar 500 µm. **b, c**, The heartbeats became faster and more regular after initiation in *tnnt2a*-MO embryos. Manually selected ROIs in the *cacna1c* morphants did not show spontaneous activity. **d – d'',** Traces of jGCaMP7f fluorescence at 0, 30, 60, and 90 minutes after onset for embryos injected with morpholinos for **d** *hcn4*, **d'** *ncx1h*, **d''** *atp1a1a* (Na^+,K^+-ATPase α-subunit). **e,** Time of onset for morphants. **f**, Mean frequency at 30 minutes post onset. **g**, Mean frequency at 60 minutes post onset. **h**, Inter-spike interval coefficient of variation (ISI CV) at a mean frequency of 0.1 Hz. *ncx1h* morphants were omitted in **c – e** because the plateaus prevented unambiguous determination of spike times. **e – h**, uninjected, *n = 39* embryos; *tnnt2a* KD, *n* = 12 embryos; *hcn4* KD, *n* = 11 embryos; *ncx1h* KD, *n* = 10 embryos; *atp1a1a* KD, *n* = 12 embryos. Uninjected

samples collected over 3 experiments, other samples collected over 1 experiment each. **e – h,** Boxplots represent interquartile range (IQR; 25th, 50th, 75th percentile) with whiskers representing 1.5x IQR. **i**, Example traces of FR-GECO1c dynamics (red) with pulsed CoChR stimulus (blue) directed to the entire heart of individual embryos. **j**, Stimulus-triggered average of calcium activity in control (blue) and *cacna1c* morphants (orange, population mean ± SD). **i**, **j**, *tnnt2a* KD, n = 11 embryos, *cacna1c* KD, n = 14 embryos. All recordings acquired at 10 Hz. All embryos were *zACNE20-myl7:FRGECO1c-P2A-CoChR-eGFP* (+/-) injected with FR-GECO1c mRNA. Statistical test values: **e – h,** Mann-Whitney-Wilcoxon two-sided test with Benjamini-Hochberg correction. (**e**) uninjected vs. *tnnt2a*, p = 0.0775; uninjected vs. *hcn4*, p = 0.11; uninjected vs. *atp1a1a*, p = 1.23e-3; uninjected vs. *ncx1h*, p = 0.0847. (**f**) uninjected vs *tnnt2a*, p = 0.149; uninjected vs. *hcn4*, p = 0.228; uninjected vs. *atp1a1a*, p = 2.11e-5. (**g**) uninjected vs. *tnnt2a*, p = 0.096; uninjected vs. *hcn4*, p = 0.256; uninjected vs. *atp1a1a*, p = 7.71e-7. (**h**) uninjected vs *tnnt2a*, p = 0.0158; uninjected vs. *hcn4*, p = 0.165; uninjected vs *atp1a1a*, p = 0.376.

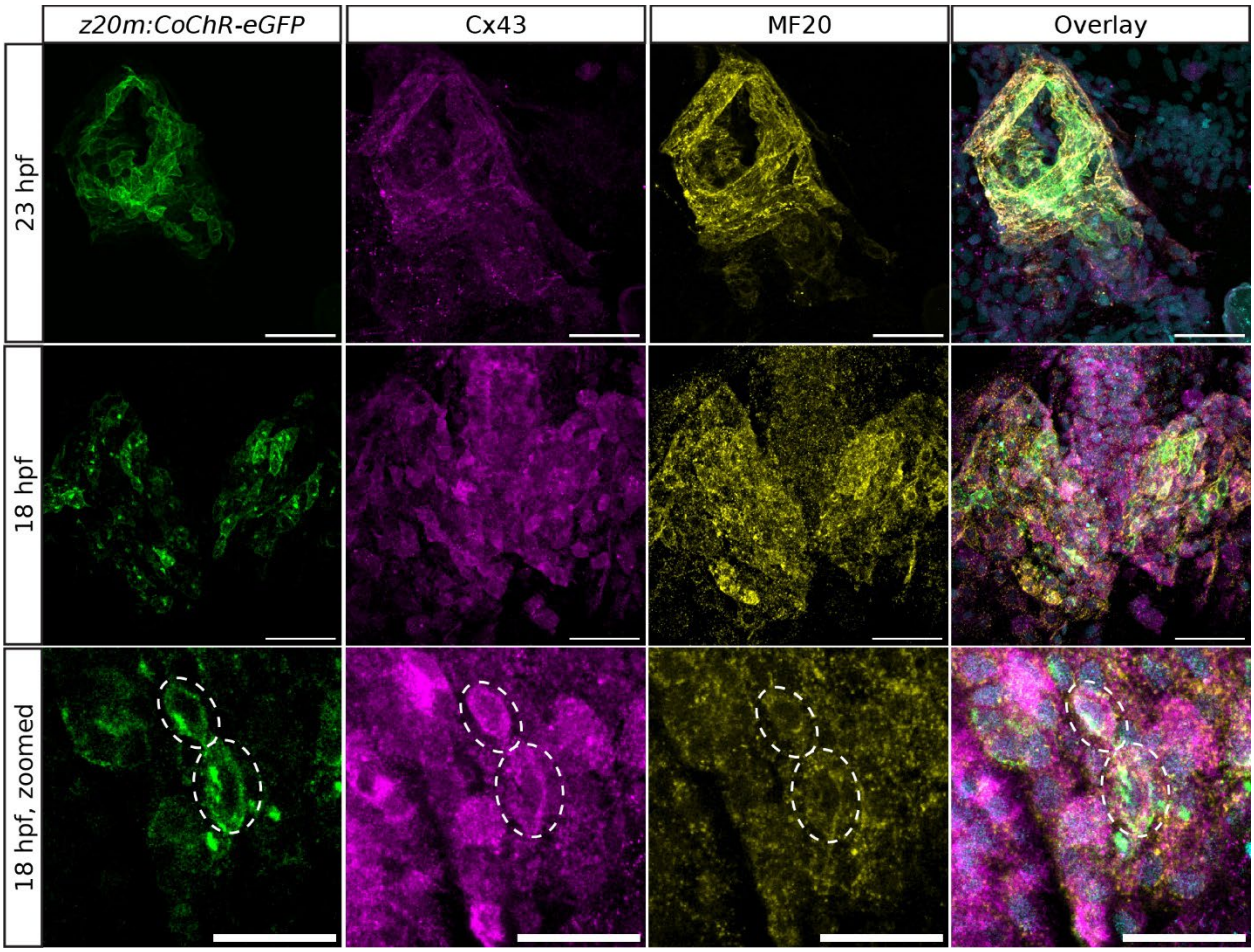

Extended Data Fig. 8: Connexin-43 is expressed in the cardiac primordium before fusion. *Tg*(*z20m:FRGECO1c-P2A-CoChR-eGFP*) fish were immunostained for connexin-43 and sarcomeric myosin (MF20). Examples of triple-positive cells indicated by dotted circles on the bottom row. Top row: 4/4 embryos over 1 experiment. Middle and bottom rows: 6/6 embryos over 3 experiments (same individuals as Extended Data Fig. _d). Cyan in overlay: nuclear staining by SYTOX Blue. Scale bars 50 µm (top and middle row), 25 µm (bottom row).

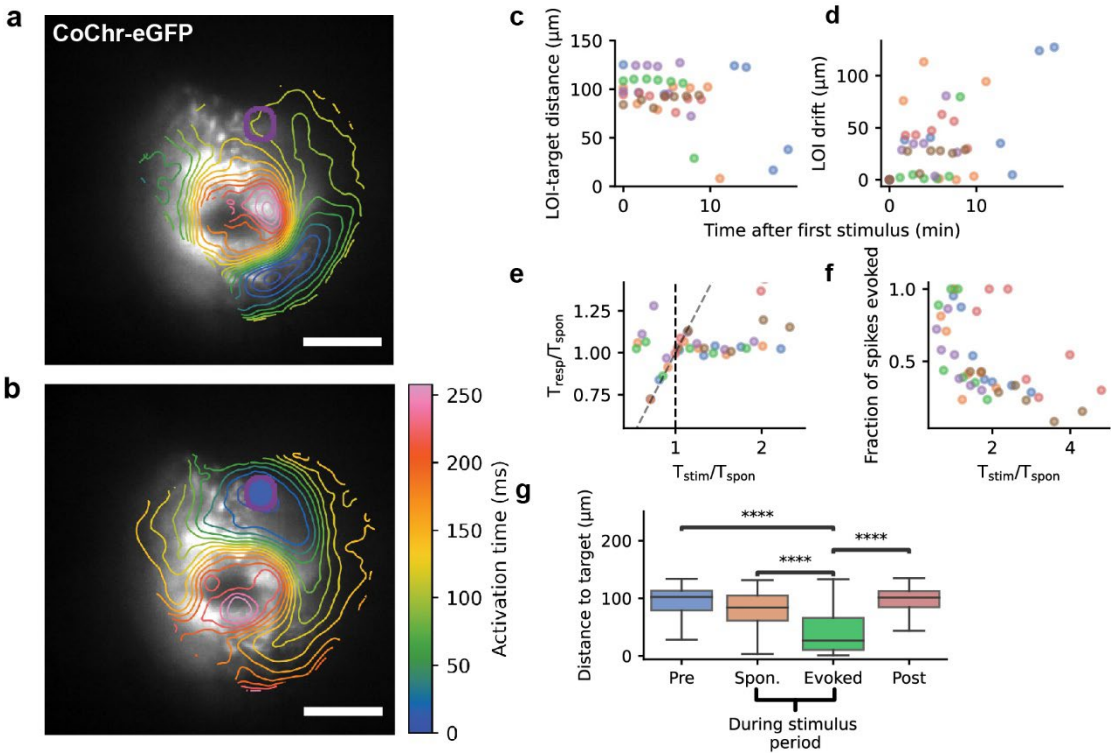

Extended Data Fig. 9: Optogenetic pacing induces overdrive suppression in the heart cone. **a**, Activation map of spontaneous activity (spike-triggered average, n = 9 spikes) in *Tg(z20m:FRGECO1c-P2A-CoChR-eGFP)* embryo. Purple circle indicates region to be stimulated in (**b**). **b**, Activation map of evoked activity (spike-triggered average, n = 19 spikes) in the same heart as (**a**). Scale bars 50 µm. **c**, Distance between spontaneous LOI and fixed "target region" after repeated pacing at different frequencies at the target region. **d**, Drift of the spontaneous LOI from its first recorded position was uncorrelated with repeated pacing. **e**, A target region away from the spontaneous LOI was paced with period T_{stim}. Heartbeat was characterized by T_{spon} = period of spontaneous activity in absence of stimulus, and T_{resp} = period of activity during periodic stimulus. CoChR activation only paced the heart (i.e. $T_{resp}/T_{stim} \approx$ `1) when` $T_{stim} < T_{spon}$. At the highest stimulus frequencies, the heart showed a period doubling, i.e. $T_{resp}/T_{stim} \approx$ `2.` **f**, Ratio of number of evoked spikes to number of total spikes (spontaneous + evoked) during the 30-second stimulus period. At a lower pacing interval, evoked spikes comprised a larger fraction of the total. "Evoked spikes" were defined as spikes which occurred within 200 ms of a pulse of blue light. (**c** – **f**) Each color represents one fish. **g**, Distance between the target region and the LOI of each individual spike grouped by timing and whether the spike was evoked. Evoked spikes had LOI significantly closer to target than any other category. Boxplot represents interquartile range (IQR; 25th, 50th, 75th percentile) with whiskers representing 1.5x IQR. (**c** – **g**) Number of beats collected per category – "Pre": 306; "During": 309; "Stim": 363; "Post": 281. n = 6 embryos in one experiment. Statistical test values: Pre. vs Evoked, U = 9.2e4, p = 1.1e-47, ****; Post vs Evoked, U = 1.5e4, p = 2.3e-52, ****; Spon. vs Evoked, U = 8.6e4, p = 2.6e-33, ****. Mann-Whitney Wilcoxon two-sided test with Benjamini-Hochberg correction.

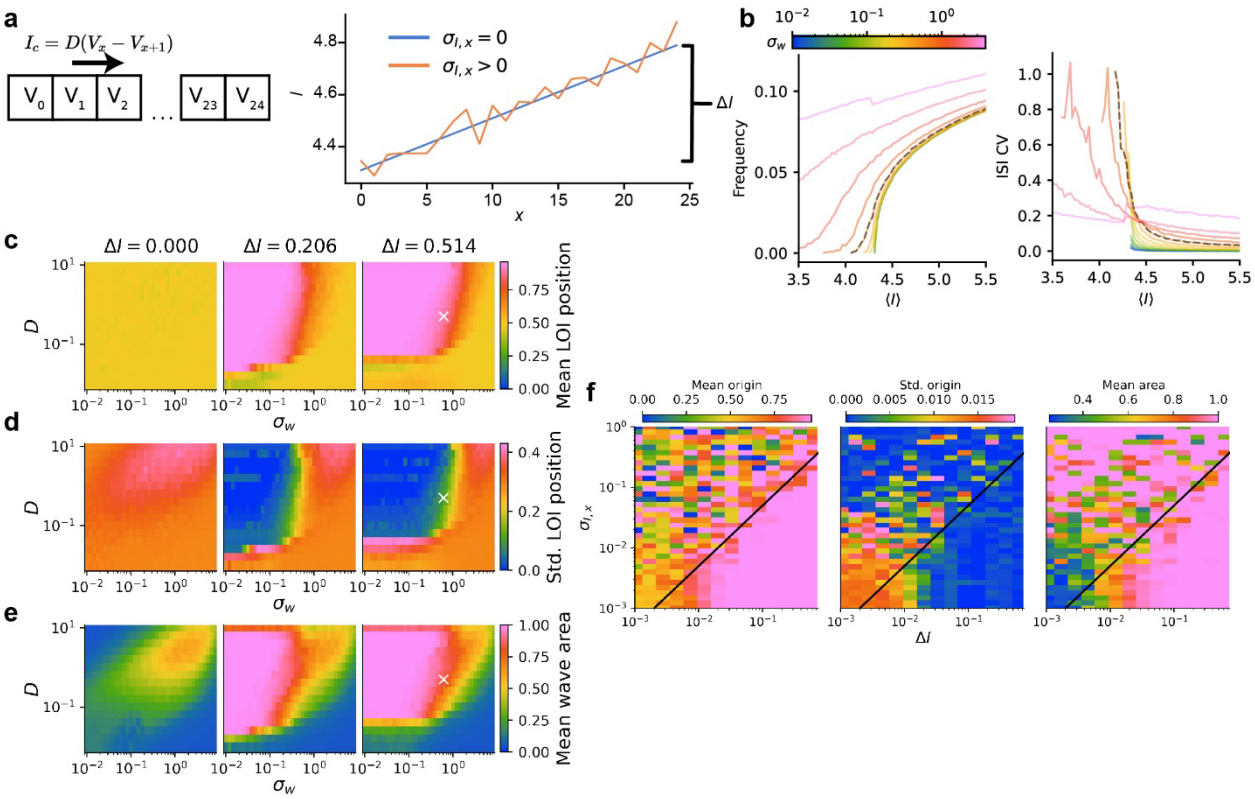

Extended Data Fig. 10: Robustness of wave geometry in heterogeneous coupled SNIC oscillators. (**a**) Schematic for chain of Morris-Lecar oscillators coupled by a current I_c which depends on coupling strength D (left); and spatial distribution of I for different choices of ΔI and $\sigma_{I,x}$ (right). (**b**) Mean frequency (f) and inter-spike interval coefficient of variation (ISI CV) for a chain of 25 oscillators with $D = 0.5$, and current gradient $\Delta I = 0.514$. Simulation with $\sigma_w = 0.618$ (compare qualitatively to experiments) marked with dashed black lines. **c** – **e**, Simulated wave properties as a function of σ_w and D. Here I attained its highest value at normalized $x = 1.0$. **c,** Normalized mean LOI position. **d,** Standard deviation of LOI position. **e**, Normalized wave area. Parameter choice for dashed line in (**b**) indicated with white "X". **f**, Wave geometry as a function of ΔI and $\sigma_{I,x}$. Black line indicates the line $\sigma_{I,x} = 0.5\Delta I$. For sufficiently large ΔI, full-tissue wave propagation occurred with stable LOI at one end of the chain. In high variability, i.e. large $\sigma_{I,x}$, a stable LOI driving full-tissue waves (low position standard deviation, high normalized mean area) can appear at positions that are not the end of the chain. (**e**, **f**) $\langle I \rangle = 4.68$, $\sigma_w = 0.03$.

Supplementary Videos

Supplementary Video 1 – Parallel measurements of heartbeat in 18 embryos. Embryos expressed jGCaMP7f and fluorescence was recorded at 10 Hz. Recording at approximately 22 hpf. Raw jGCaMP7f intensity in grayscale. ΔF/F in green. Scale bar 500 μm.

Supplementary Video 2 – **Parallel all-optical electrophysiology in 15 embryos.** Embryos expressed CoChR and FR-GECO1c ubiquitously and red fluorescence was recorded at 10 Hz. Blue light stimuli were targeted to hearts but are indicated as offset blue dots (bright when illuminated) for clarity. Recording at approximately 22 hpf. Brightfield image in grayscale. Scale bar 500 μm.

Supplementary Video 3 – Calcium dynamics before observable mechanical contractions. Brightfield (left) and jGCaMP7f (right) videos taken consecutively at 10 Hz (20 – 21 hpf). Playback at 2X speed. Scale bar 50 μm.

Supplementary Video 4 – Calcium dynamics with mechanical contractions. Brightfield (left) and jGCaMP7f (right) videos taken consecutively at 10 Hz on the same embryo as Movie S3, 1 hour later. Playback at 2X speed. Scale bar 50 μm.

Supplementary Video 5 – The first heartbeat at cellular resolution. Two Tg(*zACNE20:2x:Lyn-mCherry*) (red) embryos expressing jGCaMP7f (cyan) imaged at ~3 Hz. Videos are synchronized by the first detected heartbeat. Scale bar 50 μm.

Supplementary Video 6 – Simultaneous calcium and voltage imaging in the zebrafish heart cone. Two Tg(*zACNE20-myl7:Voltron1-P2A-jGCaMP7f*) embryos at estimated 15 minutes and 105 minutes after onset, imaged at 20 Hz, spike-triggered average. jGCaMP7f ΔF/F in green, Voltron1-JF608 ΔF/F in magenta. First principal component of jGCaMP7f ΔF/F in grayscale.

Supplementary Video 7 – Calcium wave propagation evoked by targeted CoChR activation before spontaneous cardiac activity. Tg(*z20m:FRGECO1c-P2A-CoChR-eGFP*) embryo recorded at 50 Hz. CoChR-eGFP in grayscale. FR-GECO1c ΔF/F in red. Blue light stimulus in blue. Recording at approximately 19.5 hpf. Scale bar 50 μm.

Supplementary Video 8 – Heart cone rotation and elongation. Tg(*zACNE20:2xLyn-mCherry*) embryo recorded every 10 minutes. Recording starts 21 – 22 hpf. Scale bar 25 μm.

Supplementary Video 9 – Optogenetic hyperpolarization transiently perturbs calcium wave geometry and locus of initiation. Tg(*-36nkx2.5:ZsYellow*) embryo expressing gtACR2 and FR-GECO1c. Two consecutive 50 Hz recordings with different targets for optogenetic silencing. ZsYellow in grayscale. FR-GECO1c ΔF/F in red. Blue light stimulus in blue. Recording at approximately 21 hpf. Baselines set separately for blue-illuminated intervals (separated by white frames). Scale bar 50 μm.

Supplementary Text

Image analysis

Supporting models

Dynamical bifurcations arise throughout biology[2–5]. We studied bifurcations of excitable systems to explain the temporal statistics of heartbeat initiation and the onset of propagating waves. We used three models: A) the Morris-Lecar model[6]; B) the quadratic integrate-and-fire (QIF) model[7]; and C) a spatially extended system of diffusively coupled Morris-Lecar oscillators. These models demonstrate respectively: A) that the early heart rate and variability corresponds to a saddle-node on invariant-circle (SNIC) bifurcation; B) the explanatory power of qualitative bifurcation types irrespective of the specific model; and C) an explanation of full-tissue oscillatory dynamics with varying locus of initiation (LOI).

(A) Comparison of spike distribution moments under different bifurcations using the Morris-Lecar model

Given the modulation of a single system parameter (codimension-1), there are only four bifurcations by which a stable equilibrium can disappear, and four bifurcations by which a stable limit cycle can appear[8]. These are as follows.

Stable equilibria can disappear or lose stability via:

- Saddle-node bifurcation
- Saddle-node on invariant circle (SNIC) bifurcation
- Supercritical Hopf bifurcation
- Subcritical Hopf bifurcation

Stable limit cycles can appear or disappear via:

- SNIC bifurcation (simultaneous with loss of stable equilibrium)
- Supercritical Hopf bifurcation (simultaneous with loss of stable equilibrium)
- Fold limit cycle bifurcation (often preceding a subcritical Hopf bifurcation)
- Saddle homoclinic orbit bifurcation (often preceding a saddle-node bifurcation)

The important properties of oscillatory dynamics which differ between these cases are the amplitude of oscillations, the ability to fire at arbitrarily low frequencies, and the presence of bistability of spiking and resting states (Supplementary Table 3). A detailed discussion can be found in refs. [8,9]. Bifurcation properties have been used to analyze the spiking properties of electrically excitable cells, including differing dependence of spike frequency of stimulus strength, observed experimentally by Hodgkin[10]. We sought to describe the spontaneous transition from excitable to spiking (as opposed to forced transition from a stable fixed point to a co-existing limit cycle), so we considered the bifurcations that describe loss of stability in equilibria.

Supplementary Table 3: Summary of dynamical features under different codimension-1 bifurcations.

	Saddle-node	SNIC	Supercritical Hopf	Subcritical Hopf
Coexistence of stable equilibrium and limit cycle oscillations	Yes	No	No	Yes
Subthreshold oscillations	No	No	Yes	Yes
Firing at arbitrarily low frequencies	No	Yes	Yes	No
Preferred firing (resonant) frequency	Yes	No	Yes	Yes
Arbitrarily small spike amplitude	No	No	Yes	No

The Morris-Lecar (ML) model was originally developed to describe the contractions of the giant barnacle muscle fiber and achieves good correspondence to experimental data while only accounting for voltage-dependent calcium and potassium currents[6]. It has since been widely used to study the spiking dynamics of excitable cells. The ML model can display all codimension-1 bifurcations in I, given appropriate choices of the other model parameters. The formulation we used is adapted from ref. [8]:

$$C\frac{dV}{dt} = I - g_L(V - E_L) - g_{Ca}m_\infty(V)(V - E_{Ca}) - g_K n(V - E_K) + \sigma_w dW_t$$

$$\frac{dn}{dt} = (n_\infty(V) - n)/\tau$$

$$j_\infty(V) = \frac{1}{1 + exp\left(\frac{j_h - V}{k_j}\right)}$$

[1]

Where C is membrane capacitance, V is membrane potential, I is input current, and g_i and E_i are conductances where i is one of the leak (L), calcium (Ca), or potassium (K) currents (note that these physiological labels are arbitrary and the model does not require specific potassium or calcium channels). m and n are the gating variables for calcium and potassium respectively, and τ is the characteristic timescale of potassium gating. J_∞, where $j \in \{m, n\}$, describes the steady-state gating function with a half-maximum at j_h and a slope factor of k_j. We assume that calcium gating dynamics are fast compared to potassium gating and voltage dynamics, and by timescale separation arrive at a two-variable system. An additional noise term is added to capture the stochastic behavior of the data: dW_t is a Wiener process step and σ_w is its standard deviation[11]. When combined with the rest of the dynamics, this means that subthreshold trajectories approach an Ornstein-Uhlenbeck process when far from the spike threshold.

To identify the bifurcation displayed by our experiments, we took the previously explored approach of comparing the spiking statistics to those generated by simulations[12]. We explored spiking dynamics under noisy forcing with physiologically realistic parameters which would generate each possible codimension-1 bifurcation in the absence of noise (Supplementary Table 2, ref. [3]). We numerically solved these equations using Euler integration with $\Delta t = 0.002$. As initial conditions we numerically solved for the fixed points of the system and added a small random

increment in V and n. In cases with more than one fixed point (saddle-node bifurcations), we chose an unstable one. We allowed the simulation to run until $t = 1000$ to exclude transient dynamics before collecting spike statistics over the following time window of $T = 50\,000$. We plotted frequency f and coefficient of variation (CV; λ) for different values of I and $0.01 < \sigma_w < 300$.

To compare the experimental data to the simulations, we performed the following linear transformations:

$$\hat{I} = a\tau + b$$

$$\hat{f} = cF(\tau)$$

$$\hat{\lambda} = \Lambda(\tau)$$

Where τ is the real time after onset of the heartbeat, $F(\tau)$ is the experimental beat frequency, $\Lambda(\tau)$ is the experimental ISI CV, and a, b, c represent free parameters of time scaling, time offset, and frequency scaling respectively. Since λ is already a dimensionless quantity, it requires no scaling.

For each value of σ_w, we jointly fit the mean and CV of experimental data for individual embryos to minimize the mean squared error of all observations τ_i over values of a, b, c:

$$\epsilon^2 = \frac{\rho}{M}\sum_{\tau_j=1}^{M}\left(f\left(\hat{I}(\tau_j);\sigma_w\right) - \hat{f}(\tau_j)\right)^2 + \frac{1}{N}\sum_{\tau_k=1}^{N}\left(\lambda\left(\hat{I}(\tau_k);\sigma_w\right) - \hat{\lambda}(\tau_k)\right)^2$$

The functions $f(\hat{I})$ and $\lambda(\hat{I})$ were obtained by linearly interpolating the simulated values. ρ is an additional scaling factor that is set manually to enforce an equal weighting between individual residuals of f and λ and to create comparable error sizes between models that generate different absolute frequencies. Experimental observations of frequency and CV at times τ_i were considered separately (τ_j and τ_k) to reflect the fact that a frequency of 0 contains information about the dynamics but does not have a defined CV. The individual residuals were normalized by the number of observations per moment to give equal weighting to the fits of CV and frequency. The fitting was performed using the AMPGO nonlinear optimization method[9], with manually tuned inequality constraints on a, b, c.

These models are highly simplified and almost certainly imperfect descriptions of the experimental observations. Furthermore, the functions for f and Λ have no closed form. Thus, it is challenging in any case to declare an adequate fit. We assigned equal error weightings to f and Λ but these could be changed to alter the relative quality of fit of the two experimental statistics.

The f vs. I and λ vs. I curves showed large differences between the bifurcations[13–15]. Only the spike statistics in the SNIC bifurcation resembled the data, as shown above (Extended Data Fig. 7). Oscillators near all other bifurcations showed a comparatively rapid transition to a non-zero frequency, followed by relative insensitivity of the frequency to I. In contrast, oscillation frequency near a SNIC bifurcation was dependent on a slow portion of the trajectory near the saddle-node point, and its residence time in this neighborhood was strongly dependent on I. Thus, the SNIC bifurcation can have arbitrarily low frequency. Furthermore, the other bifurcations

displayed $\lambda \gg 1$ near the bifurcation point[16–18], which is consistent with bursting spikes, whereas bursts did not arise in our data beyond chance rates (Extended Data Fig. 9d,e).

The SNIC bifurcation fit the data better than the other bifurcations for $1 < \sigma_w < 50$ (Extended Data Fig. 7c). At the optimal value of $\sigma_w = 22$, the ε^2 was 2- to 18-fold smaller in the SNIC bifurcation than in the other bifurcation classes and attained a minimum over all bifurcations and values of σ_w tested.

(B) Noisy QIF model

Noisy integrate and fire models have been widely analyzed to understand stochastic oscillations[19,20]. The differential equation we simulated is adapted from ref. [7]:

$$\frac{d\varphi}{dt} = \begin{cases} I + \varphi^2 + \sigma_w dW_t, & \varphi < \varphi_{max} \\ (\varphi_{reset} - \varphi_{max})\delta(t), & \varphi = \varphi_{\max} \end{cases} \quad [2]$$

where φ is the dynamic variable, I is an excitability parameter ("input current"), dW_t is an increment of the Wiener process (uncorrelated noise sampled from a Gaussian distribution), and σ_w is the noise amplitude. Simulations and fitting were performed as in (A). In all simulations $\varphi_{reset} = 0$.

Briefly, a qualitative description of the dynamics is as follows. If $I < 0$ and $\varphi < \sqrt{-I}$, φ decays to resting value $-\sqrt{-I}$ (Extended Data Fig. 8a). If $I < 0$ and $\varphi > \sqrt{-I}$, or $I > 0$, φ approaches infinity in a finite time. Practically, once φ reaches a finite value φ_{max}, it is set back to φ_{reset}, which we choose to be 0 (Extended Data Fig. 8b). Therefore, if $I < 0$, the system is asymptotically stable. If $I > 0$, sustained oscillations occur (Extended Data Fig. 8b). Strictly speaking, neither excitation nor limit cycles are possible in 1-dimensional systems, but the case-wise definition of the differential equation allows qualitatively similar behavior to be described. Specifically, the QIF model is a normal form of the SNIC bifurcation, meaning all equations undergoing a SNIC bifurcation can be transformed onto it through an appropriate change of variables, sufficiently close to the bifurcation point[7]. Consistent with this notion, the QIF model was able to qualitatively describe many of our observations. However, a model with more degrees of freedom would likely better fit the data, e.g. a biophysically realistic model accounting for experimentally measured ion channel conductances in the cell.

With $\sigma_w > 0$, spontaneous spiking can occur even when $I < 0$ (Extended Data Fig. 8c). This stretches out the increase in spike frequency $f(I; \sigma_w)$ as I is increased, and introduces a coefficient of variation (CV, $\lambda(I; \sigma_w)$) in the inter-spike intervals (ISIs) (Extended Data Fig. 9a)[18]. Given $\sigma_w > 0$, a "noisy but spontaneous" regime emerges. All three regimes (quiescent, noisy but spontaneous, and oscillatory) have clear qualitative correspondence to our data (Fig. 1f; Fig. 2 f, g). Quantitatively, ε^2 was a function of σ_w with a global minimum, which also minimized the variation of ε^2 across samples (Extended Data Fig. 9b – c). In addition to the first two statistical moments, the overall histogram of ISIs in the fitted model resembled the experimental distribution of the first twenty beats ($\sigma = 1.89$, I selected for each experimental trace from $\hat{I} = a\tau + b$ for τ corresponding to the median time post onset of the first 20 beats), but overrepresented the number

of short ISIs (Extended Data Fig. 9d). However, decreasing the value of φ_{reset}, which corresponds to introduction of a refractory period, improved this aspect of the fit. Furthermore, the QIF model and the SNIC bifurcating ML model both captured the experimental autocorrelation function of the instantaneous spike frequency, while the other models could not (Extended Data Fig. 9 e – g). This quantitatively confirms that there was minimal bursting in the initial heartbeats. These facts together demonstrate that the SNIC bifurcation is a good description of the experimentally observed dynamics and statistics.

(C) Formation of spatial structure in media of heterogeneous and noisy ML oscillators

Our single-oscillator model showed that the increase in beat frequency during development could be recapitulated by an increase in the bifurcation parameter *I*. The mobility and overdrive suppression phenomena we observed in the spontaneous LOI, in addition to prior studies of dissociated embryonic cardiomyocytes, suggested that the underlying dynamics could be generated by a spatially extended system of locally coupled oscillators. The variation of positions and trajectories across embryos suggested that, in addition to the dynamic noise described in the single-oscillator model, there is spatial heterogeneity in system parameters. The effects of spatiotemporal variability in coupled oscillator systems have been extensively studied[21–26]. Given the tissue-scale organization we observed, we explored the conditions under which coupling could cause multiple oscillators with different natural frequencies to phase lock.

To model a coupled medium of Morris-Lecar oscillators, we used the following equation:

$$C\frac{dV}{dt} = I_{tot}\left(V, n;\ \hat{\psi}_x\right) + D\nabla^2 V \qquad [3]$$

Where $I_{tot}(V, n; \hat{\psi}_x)$ is the right-hand side of the first expression in [1] given all specified parameters $\hat{\psi}_x$ at position x, and $D = g_c L^2$, where g_c is the gap junction conductance and L is the length of a cell. All other equations are as in [1]. In numerical simulations, we used a 1-dimensional chain of 25 oscillators (approximately the number of cells observed from one end of the heart cone to the other), with a linear spatial gradient in I and all other parameters $\hat{\psi}_x$ identical in each oscillator (Supplementary Table 2). We detected spikes in each oscillator and identified propagating waves by grouping adjacent oscillators that fired within a specified interval of each other.

The anterior-left localization of the spontaneous LOI, and its mobility over time, suggested that the parameter *I* had both a variation across the heart, and likely some static noise. If the cardiac progenitor cells were not electrically coupled to each other, this scenario would cause different cells to beat at different frequencies, something we did not observe.

We imposed a spatial gradient of *I* along the 25-unit chain using the SNIC parameters for the ML model. The mean-field relationships between *I* and frequency and ISI CV resembled those observed in the single-oscillator model (Extended Data Fig. 17a). To characterize the spatial

structure of the simulations, we quantified the mean and standard deviation of the wave origin position, as well as the mean number of oscillators recruited by each wave (Extended Data Fig. 17b – d). A small spatial gradient of $\Delta I = 0.514$ (compared to a rate of change $\frac{dI}{dt} = 0.288\ /h$ predicted by the single-oscillator model) was sufficient to induce consistent wave propagation across the medium from the end with higher I. This was true for large ranges of coupling strength D and noise strength σ_w, including values whose mean field statistics approximated the experimental data (Extended Data Fig. 17b–d). Furthermore, small random deviations from the linear spatial gradient of I did not affect the position of the LOI or the extent of wave propagation (Extended Data Fig. 17f). Larger deviations caused the LOI to move away from the end of the chain, but full-area waves occurred nonetheless (Extended Data Fig. 17f).

A plausible biological interpretation of these results is that a graded tissue-scale signal which promotes electrical maturation of the cardiomyocytes underlies ΔI. Initially cells are relatively similar but have some intrinsic variability to their bioelectrical properties, resulting in a spatially variable LOI. The gradient sets a directional bias which grows over time, allowing the LOI to migrate to the anterior left as cells there increase their natural frequency. With sufficiently strong electrical coupling, the LOI can be maintained at one position on the short timescale (beat-to-beat) due to overdrive suppression, even as heartbeats pass through the entire tissue.

Supplementary References

1. Bayly, P. V. *et al.* Estimation of conduction velocity vector fields from epicardial mapping data. *IEEE Trans. Biomed. Eng.* **45**, 563–571 (1998).
2. Ó Maoiléidigh, D. & Hudspeth, A. J. Effects of cochlear loading on the motility of active outer hair cells. *Proc. Natl. Acad. Sci.* **110**, 5474–5479 (2013).
3. Fussmann, G. F., Ellner, S. P., Shertzer, K. W. & Hairston Jr., N. G. Crossing the Hopf Bifurcation in a Live Predator-Prey System. *Science* **290**, 1358–1360 (2000).
4. Meeuse, M. W. *et al.* Developmental function and state transitions of a gene expression oscillator in Caenorhabditis elegans. *Mol. Syst. Biol.* **16**, e9498 (2020).
5. Noorbakhsh, J., Schwab, D. J., Sgro, A. E., Gregor, T. & Mehta, P. Modeling oscillations and spiral waves in Dictyostelium populations. *Phys. Rev. E* **91**, 062711 (2015).
6. Morris, C. & Lecar, H. Voltage oscillations in the barnacle giant muscle fiber. *Biophys. J.* **35**, 193–213 (1981).
7. Ermentrout, G. B. & Kopell, N. Parabolic Bursting in an Excitable System Coupled with a Slow Oscillation. *SIAM J. Appl. Math.* **46**, 233–253 (1986).
8. Izhikevich, E. M. *Dynamical systems in neuroscience*. (MIT press, 2007).
9. Rinzel, J. & Ermentrout, G. B. Analysis of neural excitability and oscillations. *Methods Neuronal Model.* **2**, 251–292 (1998).
10. Hodgkin, A. L. The local electric changes associated with repetitive action in a non-medullated axon. *J. Physiol.* **107**, 165–181 (1948).

11. Gutkin, B. S. & Ermentrout, G. B. Dynamics of Membrane Excitability Determine Interspike Interval Variability: A Link Between Spike Generation Mechanisms and Cortical Spike Train Statistics. *Neural Comput.* **10**, 1047–1065 (1998).
12. Salvi, J. D., Ó Maoiléidigh, D. & Hudspeth, A. J. Identification of Bifurcations from Observations of Noisy Biological Oscillators. *Biophys. J.* **111**, 798–812 (2016).
13. Juel, A., Darbyshire, A. G. & Mullin, T. The effect of noise on pitchfork and Hopf bifurcations. *Proc. R. Soc. Lond. Ser. Math. Phys. Eng. Sci.* (1997) doi:10.1098/rspa.1997.0140.
14. Bashkirtseva, I., Ryashko, L. & Schurz, H. Analysis of noise-induced transitions for Hopf system with additive and multiplicative random disturbances. *Chaos Solitons Fractals* **39**, 72–82 (2009).
15. Coullet, P. H., Elphick, C. & Tirapegui, E. Normal form of a Hopf bifurcation with noise. *Phys. Lett. A* **111**, 277–282 (1985).
16. Lee, S.-G., Neiman, A. & Kim, S. Coherence resonance in a Hodgkin-Huxley neuron. *Phys. Rev. E* **57**, 3292–3297 (1998).
17. Huaguang, G., Zhiguo, Z., Bing, J. & Shenggen, C. Dynamics of On-Off Neural Firing Patterns and Stochastic Effects near a Sub-Critical Hopf Bifurcation. *PLOS ONE* **10**, e0121028 (2015).
18. Vilela, R. D. & Lindner, B. Are the input parameters of white noise driven integrate and fire neurons uniquely determined by rate and CV? *J. Theor. Biol.* **257**, 90–99 (2009).
19. Lindner, B., García-Ojalvo, J., Neiman, A. & Schimansky-Geier, L. Effects of noise in excitable systems. *Phys. Rep.* **392**, 321–424 (2004).
20. Sacerdote, L. & Giraudo, M. T. Stochastic Integrate and Fire Models: A Review on Mathematical Methods and Their Applications. in *Stochastic Biomathematical Models: with Applications to Neuronal Modeling* (eds. Bachar, M., Batzel, J. & Ditlevsen, S.) 99–148 (Springer, 2013). doi:10.1007/978-3-642-32157-3_5.
21. Wood, K., Van den Broeck, C., Kawai, R. & Lindenberg, K. Universality of Synchrony: Critical Behavior in a Discrete Model of Stochastic Phase-Coupled Oscillators. *Phys. Rev. Lett.* **96**, 145701 (2006).
22. Yoon, Y. J. & Ibrahim, R. A. Parametric random excitation of nonlinear coupled oscillators. *Nonlinear Dyn.* **8**, 385–413 (1995).
23. Carotta, M. C., Ferrario, C., Vecchio, G. L. & Galgani, L. New phenomenon in the stochastic transition of coupled oscillators. *Phys. Rev. A* **17**, 786–794 (1978).
24. Assis, V. R. V. & Copelli, M. Collective behavior of coupled nonuniform stochastic oscillators. *Phys. Stat. Mech. Its Appl.* **391**, 1900–1906 (2012).
25. Doiron, B., Chacron, M. J., Maler, L., Longtin, A. & Bastian, J. Inhibitory feedback required for network oscillatory responses to communication but not prey stimuli. *Nature* **421**, 539–543 (2003).

26. Liu, Z.-Q. *et al.* Multiple spatial coherence resonance induced by the stochastic signal in neuronal networks near a saddle-node bifurcation. *Phys. Stat. Mech. Its Appl.* **389**, 2642–2653 (2010).